Atmospheric Dispersion Downstream a Two-Dimensional Obstacle: Experimental Evaluation of Turbulence Closure Models

Boundary-Layer Meteorology (2025) 191:15
https://doi.org/10.1007/s10546-025-00905-0

RESEARCH ARTICLE

Atmospheric Dispersion Downstream a Two-Dimensional Obstacle: Experimental Evaluation of Turbulence Closure Models

Pietro Salizzoni[1] · Sofia Fellini[2] · Hervé Gamel[1] · Massimo Marro[1] · Lionel Soulhac[1]

Received: 18 October 2024 / Accepted: 3 February 2025

Abstract
This study investigates the turbulent dispersion of pollutants in the wake of a two-dimensional square obstacle. Utilizing Laser Doppler Anemometry and Particle Image Velocimetry, we characterized the flow dynamics, identifying a recirculation zone downstream of the obstacle, marked by high shear and increased turbulent viscosity, and playing a crucial role in turbulent momentum exchange. We evaluated the turbulence kinetic energy budget, estimating its dissipation rate, and found traditional isotropy and Taylor hypothesis methods inadequate within the wake region. Furthermore, we explored pollutant dispersion from a linear source located downstream the obstacle. Analysis of mean concentration and variance revealed that the log-normal distribution is most effective for modelling concentrations within the recirculating region, while the Gamma distribution suits areas outside it. Testing various closure models for turbulent mass fluxes highlighted the limitations of the Simplified Gradient Diffusion Hypothesis model, favouring more complex closure models for longitudinal trends, though these still faced challenges with intensity estimation. The Simplified Gradient Diffusion Hypothesis model proved robust for vertical mass fluxes, with satisfactory results in turbulent diffusivity and turbulent Schmidt number calculations. The experimental results serve as a benchmark for validating numerical simulations and assessing the accuracy of closure models typically employed in pollutant dispersion modelling.

Keywords Pollutant dispersion · Turbulence closure models · Turbulence kinetic energy budget · Wind Tunnel

1 Introduction

The risk assessment of the release of harmful airborne substances in urban or industrial environments for operational purposes must rely on evaluating diverse scenarios. Chronic risk assessment involves simulating persistent pollutant releases over extended periods, thus

✉ Sofia Fellini
sofia.fellini@polito.it

[1] Ecole Centrale de Lyon, CNRS, Universite Claude Bernard Lyon 1, INSA Lyon, LMFA, UMR5509, 69130 Ecully, France

[2] Department of Environmental, Land and Infrastructure Engineering (DIATI), Politecnico di Torino, Corso Duca degli Abruzzi 24, 10129 Turin, Italy

Published online: 18 February 2025

encompassing a wide range of atmospheric conditions and spatial distributions of pollutant sources. This approach is typically applied in studies targeting urban air quality (Kakosimos et al. 2010; Soulhac et al. 2017). Conversely, managing accidental risks involves formulating potential scenarios of unintentional pollutant releases, based on factors such as source location, intensity, and meteorological conditions. This approach is the focus of studies addressing industrial risks, which are induced by sudden and unpredictable releases of toxic, flammable, or explosive pollutants (Cassiani et al. 2020; Fellini et al. 2021). In both cases, these risk assessments depend on computationally efficient modelling tools, enabling the simulation of numerous scenarios within a time frame suitable for operational needs (Soulhac et al. 2011, 2012, 2017; Fellini et al. 2020b; Li et al. 2023).

It is widely acknowledged in the scientific community that reliable simulation approaches must accurately reproduce the unsteadiness of the turbulent dynamics in atmospheric flow. This can be achieved through either Direct Numerical Simulations (DNS) or Large Eddy Simulations (LES), approaches that are, however, too computationally expensive. Consequently, simulations must forgo reproducing flow unsteadiness and instead rely on a time-averaged description of the flow. This can be obtained by adopting analytical solutions of boundary layer flows (Sabatino et al. 2008), reconstructing wind fields with algorithms relying on mass consistency (Finardi et al. 1998), or solving formulations of Reynolds-Averaged Navier–Stokes (RANS) equations coupled with various closure models (Sabatino et al. 2007).

Once the flow description is available, the statistical moments of the concentration field can be computed using various methods. These methods include analytical models (Marro et al. 2014, 2015), numerical solutions of the RANS equations for the budget of concentration statistics (usually mean and variance) (Milliez and Carissimo 2008a), and Lagrangian stochastic models (Cassiani et al. 2005; Marro et al. 2018), which can incorporate micromixing schemes to compute higher-order statistics.

These models are based on a wide variety of parametrisations of the large- and small-scale dynamics of the turbulent flow driving the dispersion process. Mathematically, these parametrisations are necessary to close the set of equations modelling the statistical moments of the momentum and mass budgets. Physically, they must be consistent with the major features characterising the dynamics of turbulent flows.

The reliability of these modelling approaches is typically assessed by comparing them with experimental data for a few target variables, most often focusing on the lower-order statistics of velocity and concentration. For example, the experimental evaluation of RANS model performance generally relies on their ability to predict average velocity distributions and turbulence kinetic energy (t.k.e). To date, only a limited number of experimental studies have focused on the individual components within the t.k.e. equation, specifically to validate the dissipation rate of t.k.e., ε. This is likely due to the challenges associated with its measurement (Baldi et al. 2004; Baldi and Yianneski 2004; Michelet et al. 1998). However, errors in predicting this term directly impact the estimation of turbulent viscosity and, consequently, the turbulent diffusivity coefficient of a passive scalar. This quantity is crucial for the closure of the advection–diffusion equation and thus for numerical simulations of passive scalar transport. We cite here as an example Poggi et al. (2006), who numerically investigated the influence of ε on the dispersion field in a vegetative canopy and demonstrated a strong dependence of the results on how ε is estimated. Moreover, several studies (Tominaga and Stathopoulos 2013; Moonen et al. 2011; Mochida et al. 2002; Rodi 1997; Xie and Castro 2006; Rossi and Iaccarino 2009a) have highlighted the limitations of RANS models in predicting the dynamics of flow and dispersion in flows characterised by a strong imbalance between the production and dissipation of t.k.e. and by the presence of persistent recirculating structures (typical of the flow in the built environment).

In addition to turbulent viscosity, another key parameter for estimating turbulent diffusivity is the turbulent Schmidt number Sc_t, which is often assumed to be constant over the whole velocity field. However, several experimental studies (Snijders et al. 1983; Koeltzsch 2000; Di Bernardino et al. 2020; Lim and Vanderwel 2023) have demonstrated spatial variations of the turbulent Schmidt number in boundary layer flows. Moreover, numerical studies have highlighted the limitations of assuming a constant turbulent Schmidt number. For instance, the works of Sabatino et al. (2007, 2008) showed that in dispersion through a group of obstacles, the turbulent Schmidt number can vary from 0.04 to 0.4 depending on the case. These investigations have led to new formulations for a local turbulent Schmidt number (Gorlé et al. 2010; Longo et al. 2019, 2020).

Peculiar critical aspects arise in the context of accidental industrial risk assessments, particularly concerning the dispersion of toxic, flammable, or odorous pollutants (Oettl and Ferrero 2017; Ravina et al. 2020). Notably, such assessments require estimating the probability of exceeding specific thresholds for toxicity, flammability, or odour perception. This, in turn, necessitates characterising the statistics of concentration fluctuations around the mean value and therefore phenomena characterised by large variety of time and space scales.

In such cases, a main focus is on the time-evolution equation of concentration variance, and notably on modelling its dissipation rate ε_c (Csanady 1967; Weil et al. 1992; Milliez and Carissimo 2008b, a). Various measurement techniques have been employed to examine the different terms comprising this equation in simple flow configurations such as the boundary layer (Raupach and Legg 1983; Stapountzis et al. 1986; Koeltzsch 2000; Fackrell and Robins 1982b; Marro et al. 2020), as well as in more complex scenarios like street-canyon intersections and wake behind an obstacle (Vinçont et al. 2000; Carpentieri et al. 2012b; Kukačka et al. 2012; Nosek et al. 2017; Carpentieri et al. 2018). Note that modelling ε_c is crucial for various approaches, including both the numerical solutions of the Eulerian formulation of the scalar variance budget (Milliez and Carissimo 2008a) and the micro-mixing schemes incorporated in Lagrangian stochastic models (Cassiani 2013; Marro et al. 2018).

In this framework, the availability of experimental wind tunnel data is fundamental for testing and validating new models and simulation results for dispersion processes, especially in complex geometries (Zhao et al. 2023). To this aim, we present here the results of an experimental study on the dynamics of the flow field and concentration around a two-dimensional obstacle, specifically a parallelepiped spanning the full width of the wind tunnel canyon. Despite its simplified nature, this geometry is representative of typical building shapes in urban environments. Unlike an urban canopy, the presence of a single two-dimensional obstacle eliminates complex interacting wakes, allowing for a clearer comparison with analytical models. This configuration has been chosen in previous experimental and numerical studies (Hunt 1971; Counihan et al. 1974; Yaghoubi et al. 1998; Yin et al. 2020; Vinçont et al. 2000; Charlwood et al. 2023) as it is characterised by a non-trivial flow field with the formation of three recirculation zones upstream, above, and downstream of the obstacle.

A first objective of this work is, therefore, to present detailed measurements of various statistical moments of the velocity field to analyse the terms of the evolving equation of t.k.e., with a focus on the estimate of the dissipation rate. The analysis includes estimates of the Eulerian macroscale and its link to the t.k.e. intensity and dissipation rate. A second objective is to present measurements of concentration and turbulent mass flux, obtained through a coupling of velocity and concentration, in order to study the validity of various closure models for the advection–diffusion equation. These same data provide access to the spatial evolution of the turbulent Schmidt number. The third objective is to perform an analysis of the different terms in the balance equation of the concentration variance, in order

to test a closure model for its dissipation rate currently adopted in operational models of pollutant dispersion.

2 The Experimental Setup

2.1 The Wind Tunnel Facility

The experiments were performed in a closed-circuit wind tunnel at the laboratory LMFA (Laboratoire de Mécanique des Fluides et d'Acoustique) at the École Centrale de Lyon. The test section of this tunnel is 8 m long, 1 m high and 0.7 m wide. Previous experimental studies (Salizzoni et al. 2009, 2011; Fellini et al. 2020a) have shown that this facility is suitable for reproducing flows (statistically) homogeneous along the transversal direction. Glass side walls and an external moving carriage allow measurements to be performed with non-intrusive instruments such as Laser Doppler Anemometer (LDA) and Particle Image Velocimetry (PIV) (Sect. 2.2). The wind tunnel is also equipped with a displacement system within the test section, which allows concentration measurements by Flame Ionisation Detector (FID) to be performed. Irwin (1981) spires with a height of 0.5 m were placed at the entrance of the test section (see Fig. 1). Square roughness elements (0.014 m × 0.014 m) arranged on a staggered configuration were on the floor of the wind tunnel, with a spacing of 0.045 m between them. The combined effect of spires and roughness produced a fully developed boundary layer with depth $\delta = 0.55$ m. Imposing a free stream velocity at the top of the boundary layer (U_∞) of 6.33 m/s, the Reynolds number based on δ was $Re_\delta = U_\infty \delta/\nu \sim 10^5$, where $\nu = 1.51 \times 10^{-5}$ m^2/s is the air kinematic viscosity at $T = 20°$ C, guaranteeing a fully turbulent flow.

To investigate the effect of a building-like obstacle, a square section bar with side $H = 0.1$ m and occupying the entire width of the wind tunnel was placed at a distance of 10δ downstream the spires. The roughness elements on the floor were removed from $5H$ upstream of the obstacle to avoid disturbances in the flow field around the obstacle.

Ethane was selected as the tracer gas because its density is similar to that of air, approximately 1.2 kg/m^3 at a temperature of 20°C and atmospheric pressure. A mixture of air and ethane was released from a linear source positioned at $x = 1.5H$ downstream of the obstacle (indicated as a red point in Fig. 1). The design of a linear scalar source that emits homogeneously along its length demands careful consideration and meticulous planning (Marro et al. 2018; Fellini et al. 2020a; Charlwood et al. 2023). The setup used in this study is identical to that tested and validated by Marro et al. (2020) in their investigation of dispersion from a ground-level source within a turbulent boundary layer. The linear source consisted of a stainless steel tube with needles, through which the gas is emitted into a cavity measuring 1 cm × 1 cm. The homogeneity of the emission across the width of the source (1 cm along the x-axis) and the entire width of the wind tunnel were verified in preliminary test by measurements of velocity and concentration statistics along the traversal direction. This feature is further discussed in Sect. 3.5.1. For a detailed description of the source design the reader is referred to Marro et al. (2020). The total air-ethane flow rate was 600 l/h, i.e. 1.67×10^{-4} m^3/s. The percentage of ethane could vary, from a minimum of 1.6% for measurements close to the source, to a maximum of 10% for measurements far from the source. The injection velocity at ground level (estimated as the ratio of the total flow rate to the source extension at street level) was around 0.024 m/s.

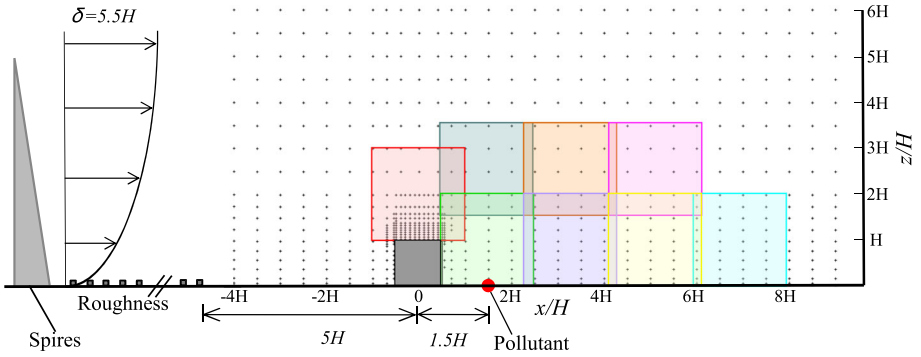

Fig. 1 Wind tunnel setup with the bidimensional obstacle. The black crosses are the measurement points for the coupled velocity-concentration measurements (FID-LDA). The colored squares represent the measurement windows of the PIV system

2.2 Measurement Techniques

The velocity field in the test section of the wind tunnel was characterized using two distinct measurement techniques: Laser Doppler Anemometry (LDA) and Stereoscopic Particle Image Velocimetry (PIV).

The LDA system was equipped with a 5 W power laser, generating two blue beams with a wavelength of λ_b = 488 nm and two green beams with a wavelength of λ_g = 514.5 nm. The beams had a diameter of 0.1 mm, and the focal length of the LDA was 400 mm. The intersection point of the four beams determined the measuring volume.

To seed the flow, olive oil was injected using an atomizer, which generated polydisperse droplets with a typical diameter of approximately 1 μm. The seeding process took place before the entrance of the wind tunnel, upwind of the location of the obstacles.

The LDA simultaneously measured two velocity components - the streamwise (u) and vertical (w) velocities - at an average frequency of approximately 1000 Hz, depending on the measurement location. The measurements were performed for 3 min to collect about 180,000 values.

To measure statistics of the transversal component of the velocity v and obtain insights on the spatial structure of the flow, we conducted a measurement campaign using Stereo PIV. Stereoscopic Particle Image Velocimetry provides the three components of the velocity field with high spatial resolution, by measuring the velocity with two CCD cameras within a region illuminated by a pulsed laser (Raffel et al. 1998; Westerweel 1997). Similar to LDA, the fluid must be homogeneously seeded with very small particles.

Stereo-PIV measurements were conducted around the two-dimensional obstacle in the $x-z$ plane. The image resolution was set at 1280 × 1024 pixels, and the observed fields covered an area of approximately 200 mm × 200 mm. Figure 1 illustrates the 8 PIV measurement planes with a side length of $2H$, yielding an average spatial discretization of $0.04H$. To ensure accurate merging of the planes, overlapping regions of at least $0.2H$ size were imposed. The interrogation window was fixed at 32 × 32 pixels with a 50% overlap. For each plane, we acquired 50,000 pairs of images (required for triple correlation measurements) at a frequency of 4 Hz.

The main source of experimental error for PIV and LDA data is due to the finite number of samples (Sciacchitano and Wieneke 2016; Salizzoni et al. 2023). Following Benedict and

Gould (1996), we considered a 95% confidence interval for the velocity statistics. For PIV measurements, we obtained an uncertainty lower than 1% for the mean velocity and for the standard deviations. Higher errors were estimated for Reynolds stress $\overline{u'w'}$ and triple correlations, respectively, 2% and 10%. The uncertainty of the LDA data assumes lower values due to a systematically larger number of samples. In any case, their magnitude is similar.

Concentration measurements were conducted using a Flame Ionization Detector (FID, HFR400 Fast FID) (Fackrell 1980), which is commonly used for measurements in urban-like geometries (Pavageau and Schatzmann 1999; Carpentieri et al. 2012a; Fellini et al. 2020a, 2022). Through a 0.3 m sampling capillary, the instrument draws in a small quantity of air and a tracer (ethane) and sends it to the combustion chamber. The calibration of the instrument was performed using ethane-air mixtures with known concentrations of 0, 500, 1000, and 5000 ppm. Calibrations were typically conducted twice a day, with additional calibrations performed if the flame temperature showed variations exceeding 2°C from the initial recorded value. The sensitivity of the instrument could vary by up to ±3%, depending on ambient conditions. Due to air recirculation in the wind tunnel, the background concentration increased over time. To account for this drift, background concentrations were recorded before and after each concentration time series. The background concentration was assumed to evolve linearly with time, ranging from its initial value to its final value. This background concentration was then subtracted from the measurement signals to account for its contribution. The instrument had a frequency response of approximately 800 Hz, therefore allowing for reconstructing the signal at a 400 Hz frequency (Nironi 2013). For each measurement point, time series of 300 s were registered, which allows up to the fourth concentration moment to be reliably estimated (see section 3.4).

To achieve measurements of turbulent mass fluxes $\overline{u'_j c'}$, a coupled LDA-FID system was used. This system enabled the simultaneous measurement of velocity and concentration within the same control volume. The set-up of the LDA-FID system, post-processing procedures, and cross-correlation analysis were thoroughly investigated in the study conducted by Marro et al. (2020). Notably, they studied several metrological aspects, such as the optimal distance between the LDA measuring volume and the FID sampling tube (4 mm) and the impact of the seed oil droplets on the estimate of the scalar statistics. The interested reader can refer to Marro et al. (2020) for more details.

In order to obtain accurate estimates of turbulent mass fluxes, both the FID and LDA instruments were operated with an acquisition time of 200 s. The effective sampling frequency of the combined system was limited by the frequency response of the FID, i.e. around 800 Hz. The measurements were performed along vertical profiles, as indicated by the black crosses in Fig. 1.

3 Results

Unless stated otherwise, all quantities are non-dimensionalised using U_∞ = 6.33 m/s as a velocity scale δ = 0.55 m as length scale and $\Delta c = Q_s \rho_s / (U_\infty \delta)$ the concentration scale, being Q_s the ethane flow rate per unit length emitted at the source and ρ_s its density. Following the Reynolds decomposition, turbulent variables, e.g. u, are expressed as the sum of their mean component $\overline{u}$ and the turbulent fluctuation u' around it. Subscripts denote the components of the vectors, and Einstein summation convention is applied, meaning repeated subscripts imply summation over their range.

3.1 First and Second Order Velocity Statistics

In this section, we present the measurements of the velocity field performed by means of PIV and LDA. The results are primarily presented in the form of four vertical profiles downstream of the obstacle at positions $x = 1.5H$, $x = 3H$, $x = 5H$, and $x = 7H$.

Figure 2a shows the streamlines above and downstream of the obstacle, overlaid on a map depicting the intensity of the average longitudinal velocity ($\overline{u}/U_\infty$) measured by PIV. Two distinct recirculation zones are clearly observed: one at the top of the obstacle and a larger one downstream the obstacle, whose farther edge is fixed by the point where the zero velocity contour ($\overline{u} = 0$ m/s) attains to the ground, i.e. approximately at $x \sim 6H$. This result is consistent with findings reported by Vinçont et al. (2000) ($x = 6.5H$ for $\delta = 7H$), Schofield and Logan (1990) ($x = 7H$ for $\delta = 7H$), and Counihan et al. (1974) ($x = 6H$ for $\delta = 8H$). The vertical profiles of $\overline{u}/U_\infty$ (Fig. 2a) demonstrate the good agreement between the results obtained from the two measurement techniques. Panels b and c in Fig. 2 present the evolution of the root mean square (r.m.s.) of the velocity components (σ_u, σ_w), while panel d shows the evolution of the Reynolds stress $\overline{u'w'}$. The discontinuity observed in the PIV results at $z = 2H$ is due to the overlapping of different measurement fields. The evolution of first- and second-order velocity statistics clearly illustrates the presence of a region in the wake of the obstacle, characterized by steep vertical velocity gradients. This region, commonly referred to as the shear layer (Townsend 1976), is where the production rate of turbulent kinetic energy is enhanced due to large mean velocity gradients, triggering Kelvin–Helmoltz instabilities. These dynamics account for the peaks in the root mean square values of both longitudinal σ_u and vertical σ_w velocity components, as well as the peaks in the Reynolds stress $\overline{u'w'}$.

Based on the Reynolds stress $\overline{u'w'}$ and the gradients of the mean velocity components, we can plot the turbulent viscosity according to the definition (Boussinesq 1877; Schmitt 2007):

$$\nu_t = -\frac{\overline{u'w'}}{\frac{\partial \overline{u}}{\partial z} + \frac{\partial \overline{w}}{\partial x}}. \tag{1}$$

The dashed red curve in Fig. 2e represents the turbulent viscosity in the undisturbed flow (see Marro et al. (2020) for further details). Just after the obstacle, at $x = 1.5H$ and for $z < 2H$, the levels of turbulent viscosity closely resemble those of the incoming flow. However, as one moves farther away from the obstacle, there is a substantial increase in turbulent viscosity within the wake region, exceeding significantly the levels observed within the undisturbed flow. This evolution of turbulent viscosity is consistent with the progressive growth of the shear layer, in line with a classical mixing-length model, which states that $\nu_t \propto \sigma_w \mathcal{L}$, being $\mathcal{L}$ the size of the largest vortices within the flow. Notably, the Kelvin–Helmholtz instabilities generated immediately downstream of the obstacle grow in size as they travel further downstream, thereby inducing a larger $\mathcal{L}$, which in turn leads to higher values of ν_t.

Based on the spatial distribution of the first- and second-order velocity statistics, we divided the flow into distinct regions. This approach is similar to the method initially presented in Salizzoni et al. (2011), albeit with slightly modified criteria, to analyze the interaction between the flow within a square cavity, the external flow above, and the shear mixing layer that develops between them at the cavity's top. The criteria adopted here for identifying these regions are as follows:

- Zone I: This region is characterized by the presence of recirculating cells. It is bounded by the downwind façade of the obstacle, the wall, and the streamline separating the two recirculating cells, one above the obstacle and the other downstream of it.

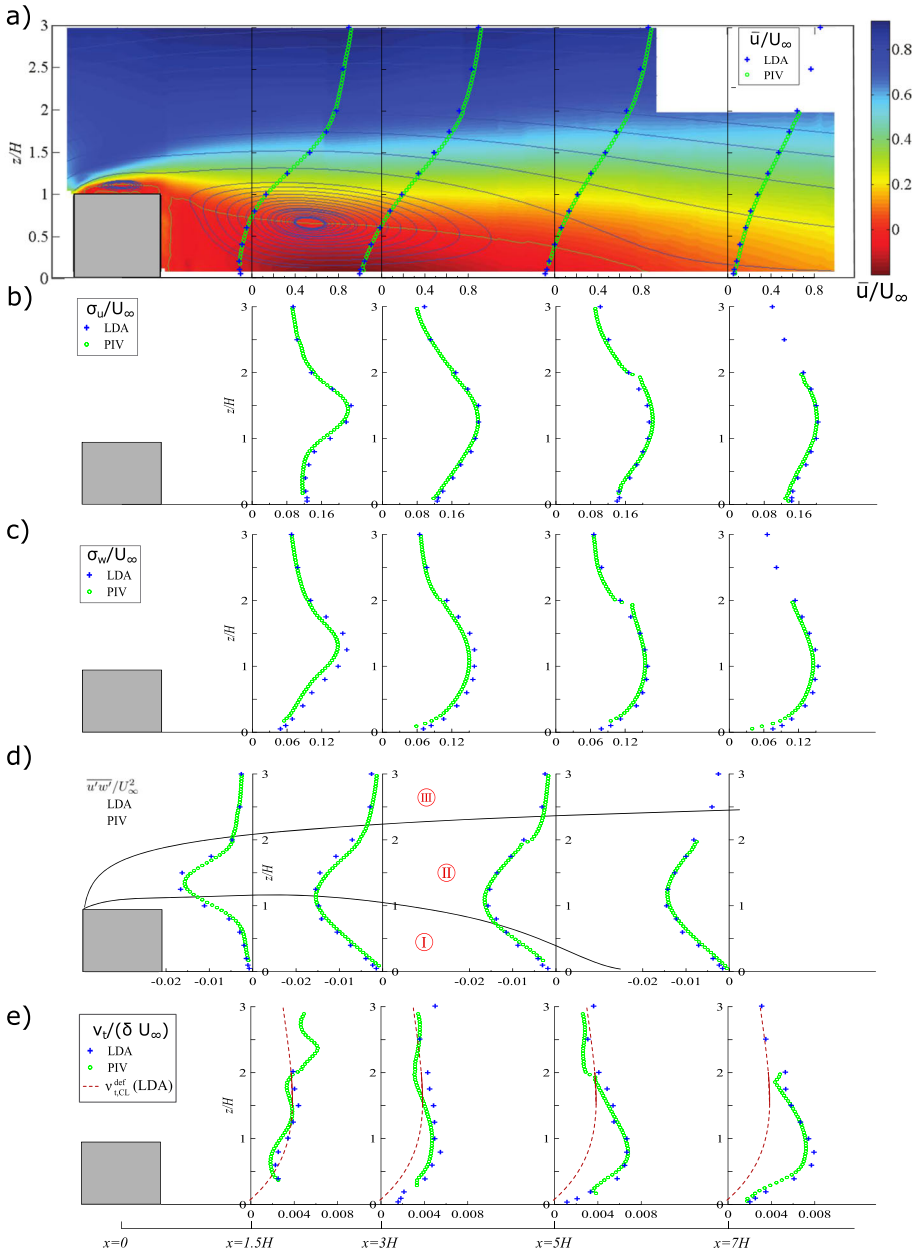

Fig. 2 **a** Velocity streamlines (blue lines), null iso-velocity lines (green lines) and horizontal velocity field ($\overline{u}/U_\infty$) measured with PIV. Vertical profiles of a) the mean horizontal velocity ($\overline{u}/U_\infty$), **b** the standard deviation of the horizontal velocity (σ_u/U_∞), **c** the standard deviation of the vertical velocity (σ_w/U_∞), **d** the Reynolds stresses ($\overline{u'w'}/U_\infty^2$), e) the turbulent viscosity ($\nu_t/\delta U_\infty$). The red dashed lines are the obtained values for a boundary layer without obstacle. In panel (**d**), the black lines delimit the different regions of the flow field

- Zone II: the central region, characterized by high turbulence kinetic energy production rate. Its lower boundary is defined by the upper limit of Zone I, while its upper boundary is determined by a threshold in t.k.e. production, specifically 10% of its maximum value, which occurs above the rod near the leading edge.
- Zone III: the outer flow region, bounded solely by the upper limit of Zone II.

3.2 Turbulence Kinetic Energy Budget

We now analyse the spatial variations of the terms composing the t.k.e. budget, which is here written for a high Reynolds number flow (i.e. neglecting diffusive fluxes) (e.g., Pope 2000):

$$\underbrace{\overline{u_j}\frac{\partial k}{\partial x_j}}_{Adv} = \underbrace{-\overline{u_i' u_j'}\frac{\partial \overline{u_i}}{\partial x_j}}_{P} \underbrace{-\frac{1}{2}\frac{\partial \overline{u_i' u_i' u_j'}}{\partial x_j}}_{T} \underbrace{-\frac{1}{\rho}\frac{\partial \overline{p' u_j'}}{\partial x_j}}_{\Psi} \underbrace{-\frac{1}{2}\nu\overline{\left(\frac{\partial u_i'}{\partial x_j}+\frac{\partial u_j'}{\partial x_i}\right)^2}}_{\varepsilon}, \tag{2}$$

where Adv represents the advection of t.k.e. (k) by the mean velocity components ($\overline{u_j}$), while the production term P represents the transfer of energy from the mean flow to the turbulent fluctuations ($\overline{u_i' u_j'}$ are the Reynolds stresses). The flux terms T and Ψ represent the transport of turbulence kinetic energy by velocity fluctuations (the term $\overline{u_i' u_i' u_j'}$ is the triple correlation of velocity fluctuations) and pressure fluctuations (p'), respectively, and ε is the average t.k.e. dissipation rate. Note that ρ and ν are the air density and kinematic viscosity, respectively.

The first three terms of the budget (Adv, P, T) can be directly estimated from the measurements by knowing the three velocity components and their spatial gradients, as well as the double and triple correlations of velocity fluctuations. The contribution of Ψ is generally assumed to be negligible in boundary layers or pipe flows (e.g.,Pope 2000), but this is not generally the case in the wake of a bluff-body. The direct estimate of ε is a challenging task as it requires capturing instantaneous velocity gradients at the Kolmogorov scale η. This would imply reducing the size of the measurement fields by an order of magnitude.

To obtain estimates of ε, we adopt in this study different approaches, each supported by a simplifying hypothesis regarding the nature of the flow. A first estimate is achieved by calculating the residual, referred to as ε_R, of the Eq. (2). Note that, due to the absence of pressure fluctuation estimates and the inability to determine Ψ, this residual is computed by omitting the contribution of Ψ, which is not necessarily negligible (Liu and Thomas 2004; Schanderl et al. 2017).

For the calculation of the various terms comprising the budget, the velocity fields obtained from PIV were initially subjected to fitting along the x and z directions, using a 3rd order polynomial function. This was done due to the potential introduction of significant errors in spatial gradient discretisation.

Figure 3a shows the terms of the t.k.e. balance obtained from the PIV measurements. In the recirculation zone and for $z > 2H$, the terms are nearly zero but become significant in the region of high shear, i.e. for $H < z < 2H$. As we move away from the obstacle ($x > 3H$) the advection term (Adv) fades out, and the dissipation term (ε) has the same intensity as the sum of the transport term (T) and the production term (P). It is also noteworthy that in the region of high shear, the production term P is stronger than the dissipation term ε, implying a transport (T) of energy towards regions with lower levels of t.k.e.

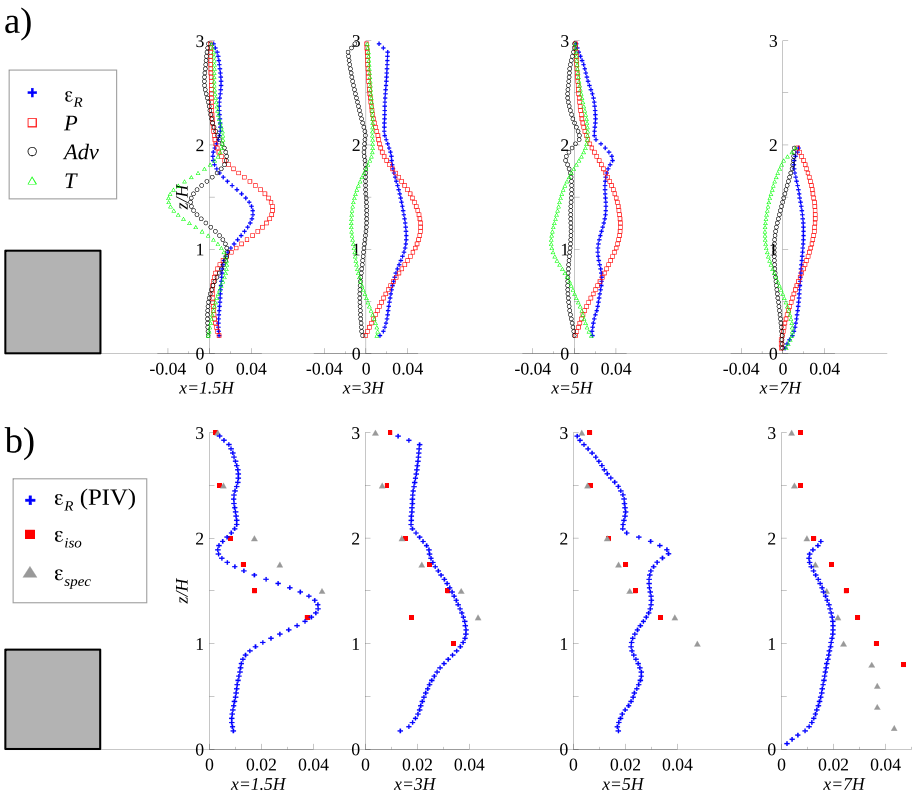

Fig. 3 **a** Terms of the t.k.e. balance downstream the obstacle. **b** Comparison of different methods to estimate ε downstream the obstacle

An alternative approach to estimate ε relies in employing the isotropic approximation and Taylor's hypothesis of frozen turbulence (Hinze 1975):

$$\varepsilon_{iso} = \frac{15\nu}{\overline{u}^2}\overline{\left(\frac{\partial u}{\partial t}\right)^2}. \tag{3}$$

Adopting the same assumptions, ε can be estimated from spectra. Indeed, the shape of the energy spectrum ($E(\kappa)$) should conform to the theory of the Richardson-Kolmogorov cascade and, in particular, exhibit an inertial range where the following relationship holds:

$$E(\kappa) = C\varepsilon^{2/3}\kappa^{-5/3}, \tag{4}$$

where the Kolmogorov constant C is 1.5 (Pope 2000). The wave number κ is related to the time frequency f as $\kappa = 2\pi f/\overline{u}$ and the conversion between frequency ($S(f)$) and wave number ($E(\kappa)$) spectra is given by:

$$\kappa E(\kappa) = f S(f). \tag{5}$$

By combining Eqs. (4) and (5), the dissipation rate of t.k.e. can be estimated as:

$$\varepsilon_{spec} = \frac{2\pi}{\overline{u}}\left(\frac{S_u(f)\cdot f^{5/3}}{C}\right)^{3/2}, \tag{6}$$

where S_u is the spectrum for the horizontal velocity component u. The implementation of the three methods is depicted in Fig. 3b. The computation of ε_{iso} and ε_{spec} is omitted within the recirculation zone downstream the obstacle, due to the almost negligible mean velocity, which undermines the assumption of frozen turbulence fundamental to these estimates. Conversely, towards the upper portion of the profiles, the three outcomes progressively align with comparable values. At the farthest downstream position, we observe significant discrepancies between ε_R and the other two estimates ε_{iso} and ε_{spec}. Notably, ε_R exhibits anomalous behaviour, tending toward zero as it approaches the wall, a trend inconsistent with similarity theory, which predicts a scaling of the form $\varepsilon \propto u_*^3/z$. This anomaly is likely due to the significant influence of the pressure–velocity correlation term, represented by Ψ in the turbulence kinetic energy budget (see Eq. 2).

3.3 The Eulerian Integral Length Scale

Another interesting piece of information for describing the flow field downwind of the obstacle concerns the turbulence spatial structures. The two-point spatial correlation of velocity components is calculated as:

$$R_{ii,l}(s,r) = \frac{\overline{u_i'(s)u_i'(s+r)}}{\overline{u_i'(s)u_i'(s)}}, \tag{7}$$

where i indicates the considered velocity component, l indicates the selected direction along which the correlation is evaluated, s represents a specific location in the flow field, and r is the separation distance along the chosen direction l. The velocity correlation functions $R_{ii,l}(s,r)$ quantifies the relationship between the velocity fluctuations at s and $s+r$ in the direction l, providing insights into the spatial coherence and organisation of turbulence structures in the flow around the obstacle. The integration of the velocity correlation function (Eq. 7) provides a correlation length, i.e. the integral length scale:

$$L_{ii,l}(s) = \int_0^\infty R_{ii,l}\,dr. \tag{8}$$

From PIV measurements, we could determine the velocity correlation functions (Eq. 7) along the x and z directions for the three velocity components (u, v, w). Figure 4 shows the velocity correlation functions $R_{uu,x}$ and $R_{uu,z}$ (panel b1), $R_{ww,x}$ and $R_{ww,z}$ (panel b2), and $R_{vv,x}$ and $R_{vv,z}$ (panels b3) for point 1 ($x/H = 1.7$, $z/H = 0.24$) located behind the obstacle, in the recirculating region. Panels d1, d2 and d3 report the same quantities for point 2 ($x/H = 5.2$, $z/H = 1.04$), located in the region of high-shear. The velocity correlation functions $R_{ii,x}$ are computed along the horizontal (blue) dashed line shown in panels a and c, while the velocity correlation functions $R_{ii,z}$ are computed along the vertical (red) dashed line. Panels a and c also display the iso-correlation lines in the (x, z) cross-section for values ranging from 0.3 to 0.8 with an increment of 0.1.

The trends of the velocity correlation functions show that the velocity components u and w are influenced by the presence of the wall and the obstacle, which break the isotropy of turbulent structures with a higher correlation along the longitudinal axis, compared to the vertical axis (panels b1, b2, d1, d2). In the recirculating zone, spatial correlations of the vertical (w, panels a2, b2) and transverse (v, panels a3, b3) velocity components are very limited, whereas they extend over longer distances in the shear zone (panels c2, c3, d2, d3), where a tilt of coherent structures toward the stream-wise direction is also observed (panel c2).

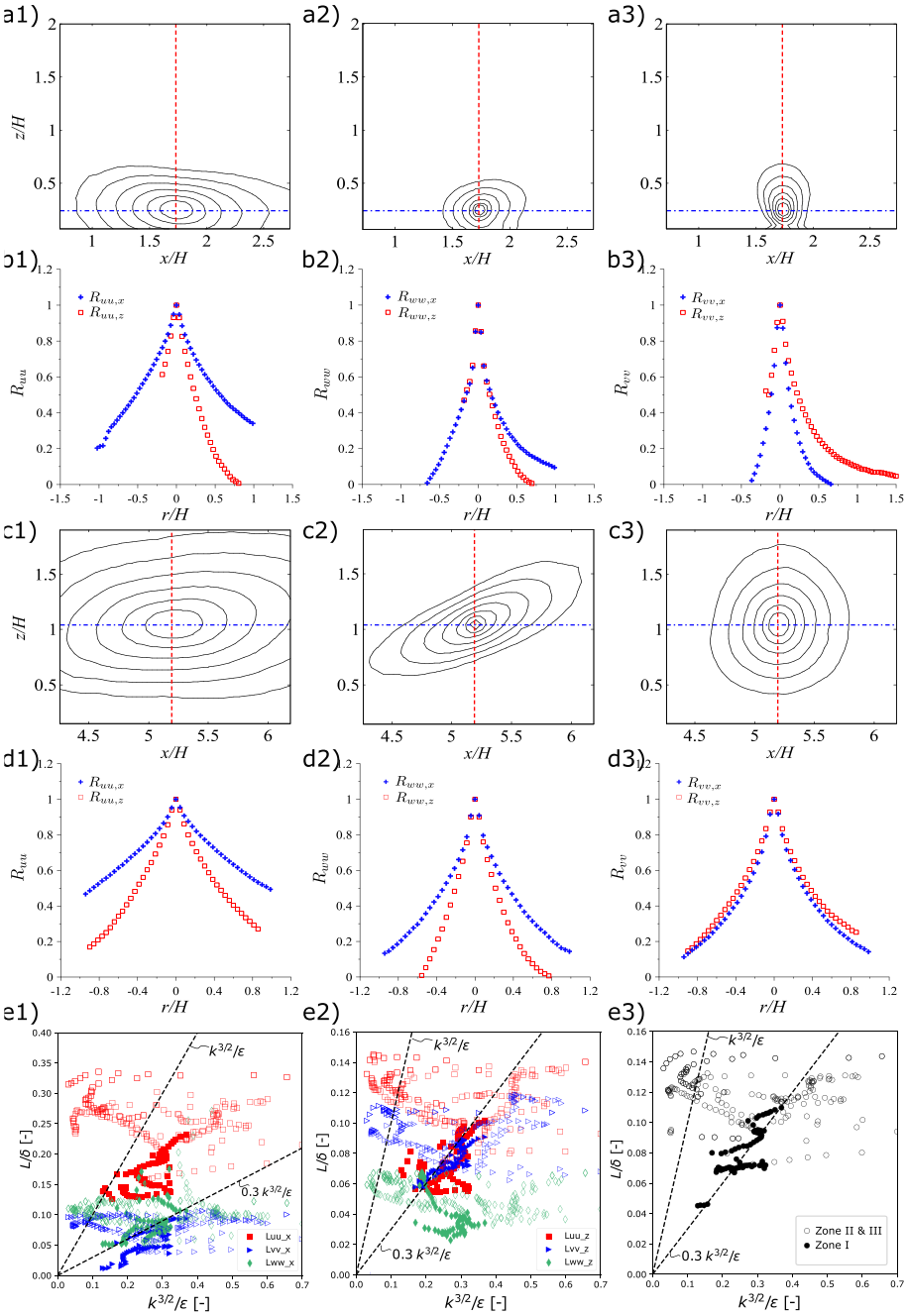

Fig. 4 **a** Iso-correlation lines in the x, z cross-section and **b** velocity correlation functions for point 1 ($x/H = 1.7$, $z/H = 0.24$), computed along the horizontal (blue) and vertical (red) dashed lines reported in panels a. **c** Iso-correlation lines in the x, z cross-section and **d** velocity correlation functions for point 2 ($x/H = 5.2$, $z/H = 1.04$), computed along the horizontal (blue) and vertical (red) dashed lines reported in panels b. **e** Verification of the existence of a linear relationship between (e1) $L_{ii,x}$, (e2) $L_{ii,z}$, (e3) L_{iso} and $k^{3/2}/\varepsilon$. The data represented correspond to all measurement points at positions $x = 1.5H$, $x = 3\,H$, $x = 5\,H$, and $x = 7.5H$. Solid markers represent points situated within the recirculating region (Zone I), while empty markers denote points outside of it (Zone II and III)

Starting from these results, we can estimate the integral length scale according to Eq. (8). In order to reduce uncertainties arising from the numerical estimate of the integral, we assume that the velocity correlation function can be modelled as an exponential function:

$$R_{ii,l}(s,r) = e^{-|r|/\Lambda_{ii,l}}. \tag{9}$$

Given Eqs. (8) and (9), we obtain that $L_{ii,l} = \Lambda_{ii,l}$, and the values of the length scales can be inferred from the measured correlation functions by fitting the exponential curves to the data (Tritton 1974). Note that this procedure is analogous to estimating the Eulerian integral length scales as the distance at which the correlation function decreases below a specified threshold value $R_{ii,l} = e^{-1} \simeq 0.37$ (Nironi et al. 2015). Similar approaches have been employed by Bewley et al. (2012) and Takimoto et al. (2013), who used threshold values of 0.4 and 0.5, respectively.

Assuming local dynamical equilibrium, where the kinetic energy flux transferred by large turbulent structures in the energy cascade is entirely dissipated locally by molecular viscosity, dimensional analysis shows that the relationship between the large-scale size, turbulence kinetic energy intensity, and its dissipation rate must take the following form:

$$L_{iso} \sim k^{3/2}/\varepsilon, \tag{10}$$

where L_{iso} represents a characteristic integral length scale and the dissipation is estimated as $\varepsilon = \varepsilon_R$. Such a relationship is often adopted as an estimate of the Eulerian scale for analytical (Marro et al. 2015) and stochastic (Cassiani et al. 2005; Cassiani 2013; Marro et al. 2018) pollutant dispersion models. It is also commonly adopted in the formulation of the $k-\varepsilon$ closure model, where the turbulent viscosity is computed as the product of a velocity scale and a length scale computed through Eq. (10) (Launder and Spalding 1974; Comte-Bellot and Bailly 2003).

To test Eq. (10), we present in panels e1 and e2 of Fig. 4 the values of the integral length scales $L_{uu,x}$, $L_{vv,x}$, $L_{ww,x}$, $L_{uu,z}$, $L_{vv,z}$, and $L_{ww,z}$ as a function of the ratio $k^{3/2}/\varepsilon$, calculated for measurement points at $x = 1.5H$, $3\,H$, $5\,H$, and $7\,H$ with z/H ranging from 0 to 3. It is noticeable that the integral scales along the z-axis (panel e2) have significantly lower values compared to those along the x-axis (panel e1), the main wind direction. Panels e1 and e2 illustrate that the dispersion of points is significant. In panel e3, the scale L_{iso} is reported for each measurement point, calculated as the mean value of the aforementioned six scales. Solid markers denote points located within the recirculation zone behind the obstacle (Zone I), while empty markers indicate points outside of it (Zone II and III). In general, we observe poor agreement between our experimental data and the functional form provided by Eq. (10). Within the recirculation zone, a linear trend between L_{iso} and the ratio $k^{3/2}/\varepsilon$ can be identified, with a slope of approximately 0.3. However, outside zone I, it becomes challenging to establish a clear one-to-one relationship linking the Eulerian integral scale L_{iso} and the ratio $k^{3/2}/\varepsilon$. This discrepancy can be attributed to the varying influence of turbulence kinetic energy (t.k.e.) transport terms within the velocity field, which disrupt the balance between production and dissipation, thereby undermining the applicability of Eq. (10).

3.4 The Concentration Field

Figure 5a shows a map of the dimensionless average concentration $\overline{c}^*$, representing the dispersion of pollutants from the ground-level source (placed at $x = 1.5H$). In the recirculation zone, it can be observed that the pollutant is transported from the source towards the obstacle, then it travels upward along the downstream face until reaching the top, before being carried

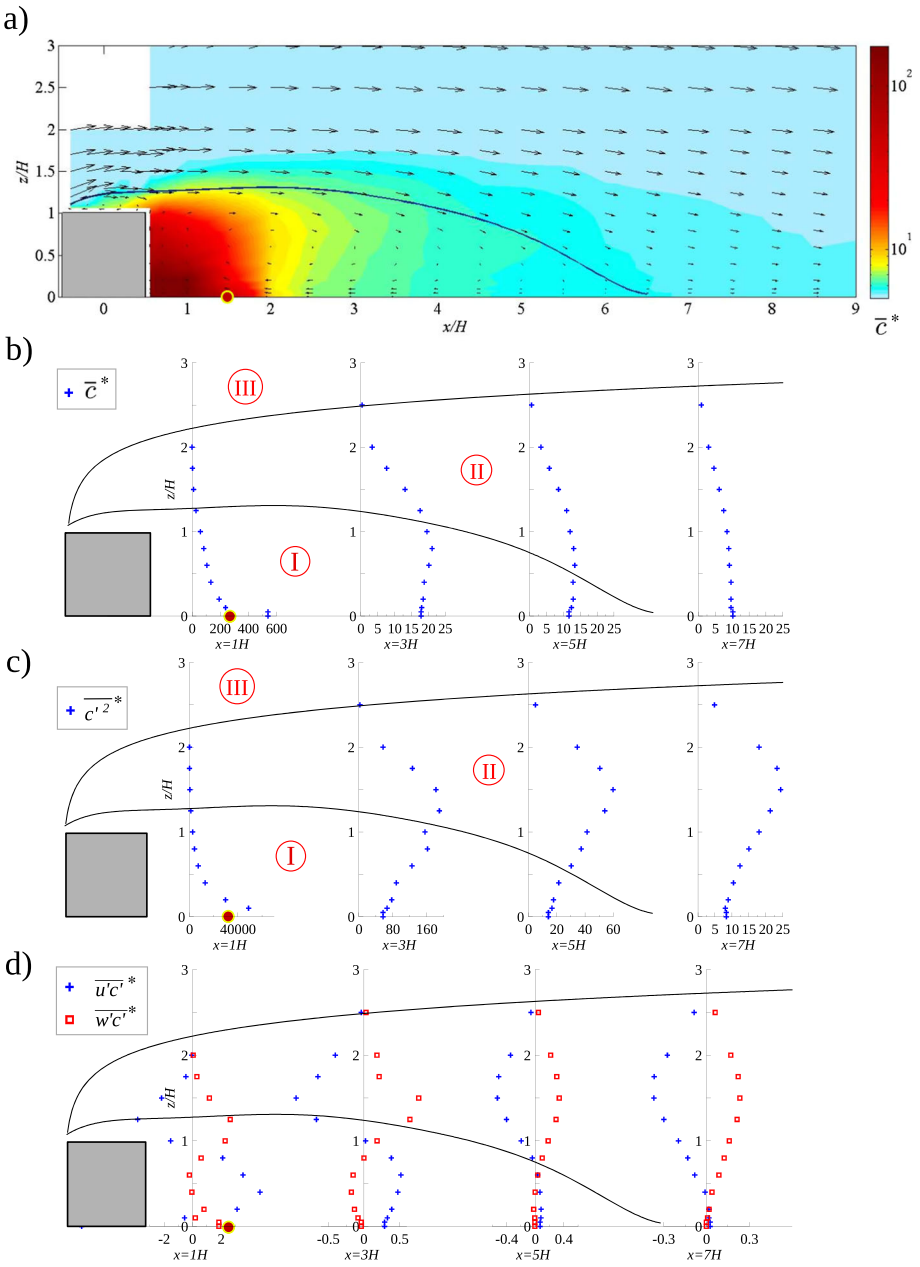

Fig. 5 **a** Mean concentration field ($\overline{c}^*$ in logarithmic scale). Arrows represent the velocity vector field while the blue line delimits the recirculation zone. Vertical profiles of **b** the mean concentration ($\overline{c}^*$). **c** the concentration variance ($\overline{c'^2}^*$), d) the horizontal ($\overline{u'c'}^*$) and vertical ($\overline{w'c'}^*$) turbulent mass fluxes downstream the obstacle. The black lines delimit the different regions of the flow field

along the boundary of the recirculation zone. At this point, the pollutant is either transferred to the external flow or remains trapped within the recirculation zone. It is also noteworthy that a portion of the pollutant is transported into the recirculation region located above the obstacle. These phenomena are well shown also in Fig. 5b that presents the vertical evolution of the dimensionless average concentration $\overline{c}^*$. The partitioning of the domain into the three zones identified when analysing the velocity field remains relevant for the dispersion process: Zone I represents the recirculation bubble trapping the scalar just downstream the obstacle; Zone II is the intermediate region of intense scalar fluxes of the concentration from Zone I to Zone III, which refers to the external flow.

Figure 5c reports the evolution of the dimensionless concentration variance $\overline{c'^2}^*$ in the wake of the obstacle. Between the obstacle and the pollutant source ($0.5H < x < 1.5H$), the maximum intensity of the concentration fluctuations is very high and occurs at ground level, indicating the proximity of the source. Beyond the position of the source ($x > 1.5H$), there is a significant decrease in the values of $\overline{c'^2}^*$ by two orders of magnitude, dropping from 10^4 to 10^2. The region II is characterised by high levels of concentration variance, caused by the alternating passage of 'clean' air eddies coming from the external flow field (Zone III) and eddies carrying large amount of scalar, ejected from the recirculation region (Zone I).

Figure 5d shows the turbulent mass fluxes, both longitudinal and vertical, in the wake of the obstacle obtained through the coupling of LDA-FID techniques (see Sect. 2.2). In the recirculation region (Zone I), the vertical flux is much smaller compared to the longitudinal flux. An increase in the intensity of the turbulent vertical flux is observed at the boundary between Zones I and II, indicating the scalar transfer from Zone I to Zone II.

In addition to mean and variance concentration fields, it is valuable to explore the probability distribution function (pdf) of concentration fluctuations. This is essential because various applications related to health risk assessment for exposure to toxic substances and odour evaluation rely on assessing the occurrence of extreme pollutant values.

A key focus in investigating scalar concentration statistics is identifying an appropriate model for the one-point pdf. The chosen distribution typically exhibits three main characteristics: (i) it is constrained to positive values, (ii) it is fully determined by the ratio of the two lowest concentration moments, specifically the fluctuation intensity $i_c = \sqrt{\overline{c'^2}}/\overline{c}$, and (iii) it shows significant shape variations depending on the value of i_c, notably including positive skewness for large i_c.

Previous research has predominantly focused on the probability density function resulting from localized releases, commonly referred also to as 'point' sources (Cassiani et al. 2020), i.e. whose size is much smaller than the distances over which the dispersion process is observed. Nironi et al. (2015) observed that the experimental pdf changes with distance from the source and is well represented by a gamma distribution. This result was recently confirmed by Lim and Vanderwel (2023), who, however, noted that the accuracy of the Gamma distribution decreases at the plume edges, where the concentration pdf is better represented by a Lognormal distribution, as also suggested by other studies (Yassin 2008; Finn et al. 2010). Concentration percentiles derived from the Weibull distribution are commonly used in odour assessment (Oettl and Ferrero 2017). Regarding line sources, Li and Bilger (1996) found that the experimental pdf is right-skewed near the source and approximates a symmetrical Gaussian distribution in the distant field. In a recent study, Del Ponte et al. (2024) investigated the pdf distribution of a passive scalar released from a line source in a street canyon, concluding that the Lognormal distribution is the most appropriate model.

Following the same analysis proposed by Del Ponte et al. (2024), we evaluate in this study which of the Gamma, Lognormal, or Weibull distributions is the best model for pollutant

concentration downstream of the obstacle. To compare the probability density functions calculated at different points, we employ the non-dimensional variable $\chi(t) = c(t)/\overline{c}$. In this way, the analytical functions of the three aforementioned pdfs can be expressed in terms of a single parameter, $i_c = \sqrt{\overline{c'^2}}/\overline{c}$, the concentration fluctuation intensity. Panel a in Fig. 6 shows that i_c is less than 1 (filled markers) in the recirculation region (Zone I) downstream of the obstacle, as well as in the high shear region far from the source (see trends at $x = 5H$ and $x = 7H$). The shape of the pdfs (panel d) in this case is rather symmetric but with a short right tail, and it is well approximated by a Lognormal distribution. This shape is typical of a turbulent dispersion-governed transport process. In the upper part of the high shear region, mean concentrations tend towards zero, but pollutants are occasionally transported through large-scale fluctuations. In this case, i_c is greater than 1 (empty markers in panel a), and the exponential shape of the distribution (panel b) can be modelled by a Gamma or Weibull function. When i_c approaches 1, the distribution's shape is intermediate between the two (panel c).

To assess the suitability of the different distributions to fit the data, we compared the skewness and kurtosis obtained from the analytical distributions as a function of i_c (see Del Ponte et al. 2024 for details about the functions) with those directly obtained from the experimental data. In the recirculation zone (panels e-f), the scatterplots show a good fit by the Lognormal function. The only exception is the single point characterized by $i_c > 1$ (empty marker), which is located at the interface between regions I and II at $x = 1H$ (see panel a). For this point, Gamma and Weibull distributions present a better agreement. In region II, on the other hand, the Gamma distribution fits well for points with both $i_c >= 1$ and $i_c < 1$ with respect to the Lognormal distribution, as it adapts its shape based on this parameter. The Lognormal distribution also exhibits a reasonable fitting capacity for points with $i_c < 1$ in this area. Even if the Weibull distribution presents a behaviour similar to Gamma model changing its shape depending on the value of i_c, the comparison with the experimental results is generally poor.

3.5 Closure Models for Turbulent Mass Fluxes

In this section, we analyse the consistency of different closure models for the turbulent mass fluxes in the advection–diffusion equation. We examine both the longitudinal and vertical fluxes and apply the most renowned models: Standard Gradient-Diffusion Hypothesis (SGDH), Generalized Gradient-Diffusion Hypothesis (GGDH), and the Higher Order Generalized Gradient-Diffusion Hypothesis (HO-GGDH). A comparable investigation was carried out by Rossi and Iaccarino (2009b) using the experimental profiles measured by Vinçont et al. (2000) downstream of a two-dimensional square obstacle. In Rossi and Iaccarino (2009b), constant values of $\alpha_c^{GGDH} = 0.1$ and $\alpha_c^{HO-GGDH} = 0.2$ were established for the GGDH and HO-GGDH models. In analogous studies related to scalar dispersion across a shear flow (Rossi 2010) and around a cube (Rossi et al. 2010), these constants were estimated to be $\alpha_c^{GGDH} = 0.3$ and $\alpha_c^{HO-GGDH} = 0.575$, respectively. In the subsequent sections, we assess the validity of these various models and the associated constant values using our more comprehensive database.

3.5.1 Horizontal Scalar Fluxes

The downstream evolution of the mass flux $\overline{uc}$ components, including the mean term $\overline{u}\,\overline{c}$ and the turbulent $\overline{u'c'}$ counterpart is depicted in Fig. 7a. The vertical variations of the mean and

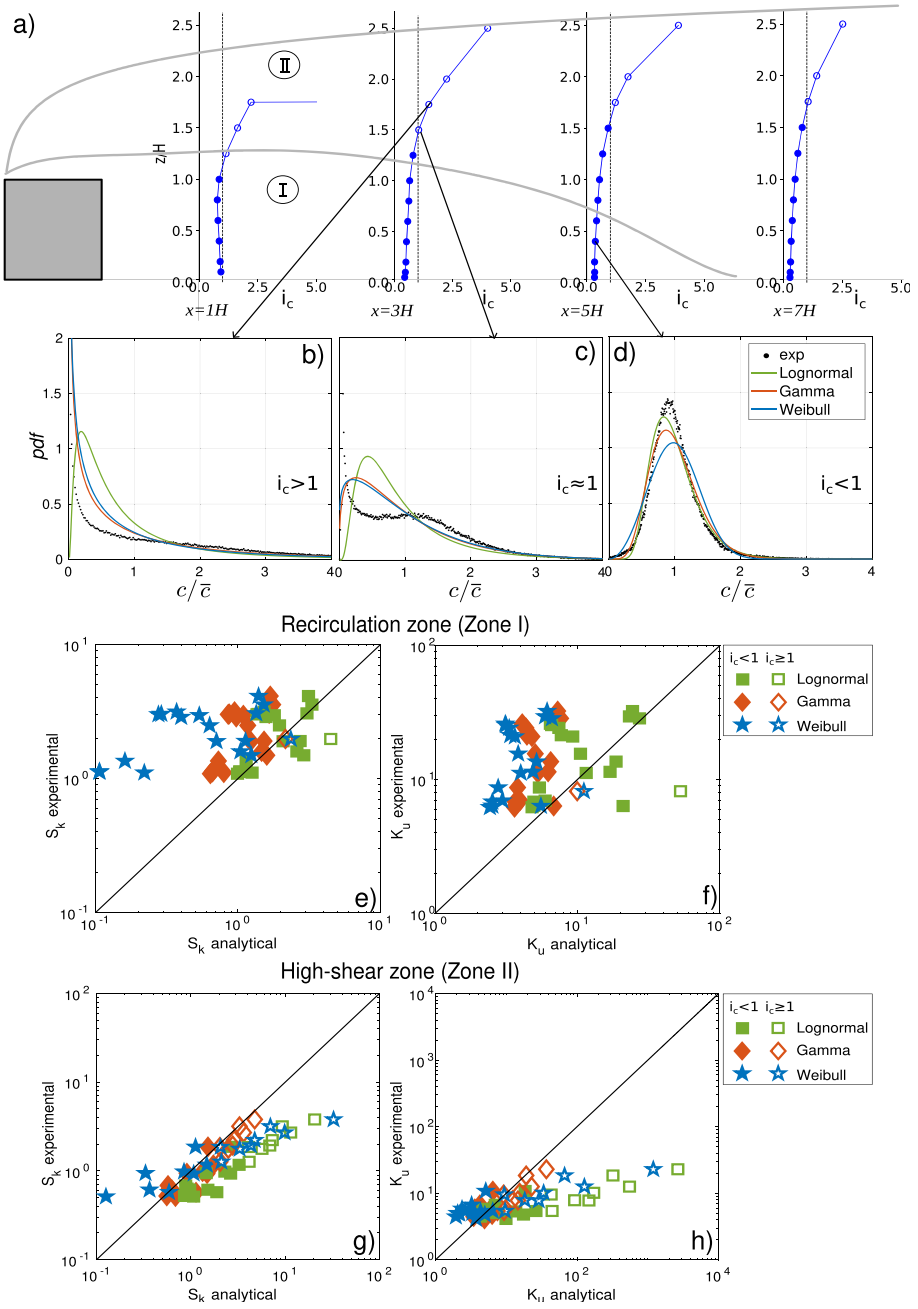

Fig. 6 **a** Spatial evolution of the concentration fluctuation intensity i_c. Concentration pdf for b) $i_c > 1$, c) $i_c \approx 1$, **b** $i_c < 1$. Scatterplots that compare analytical and experimental skewness (S_k) and kurtosis (K_u) in the recirculation zone (**e**,**f**), and in the high-shear zone (**g**,**h**). Empty markers represent the points characterized by $i_c > 1$

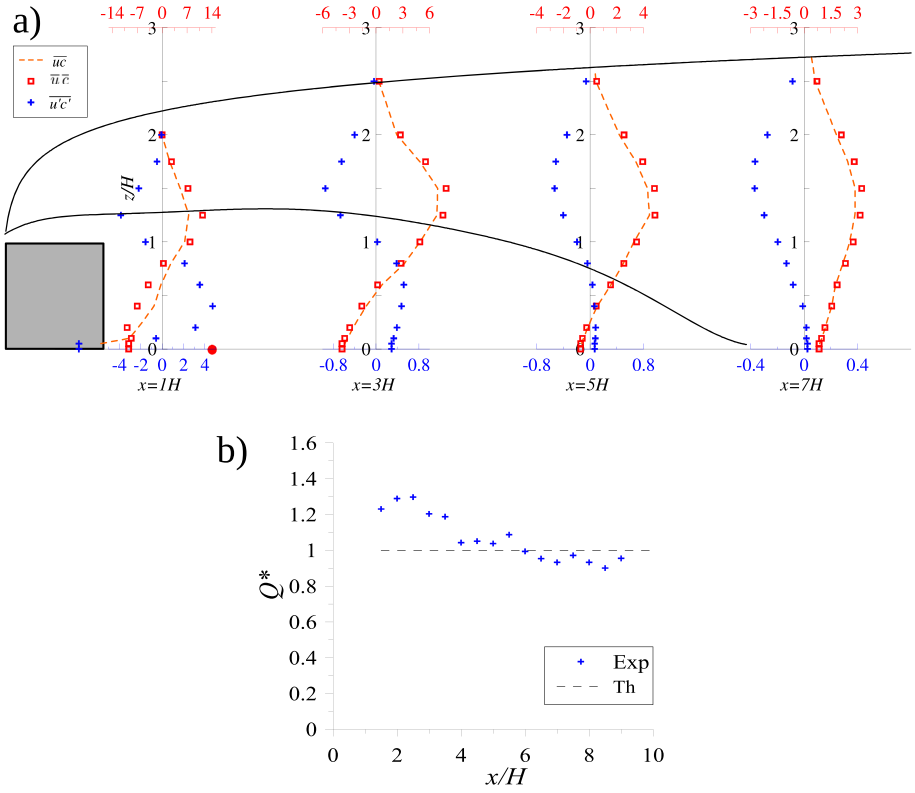

Fig. 7 **a** Downstream evolution of the mass flux $\overline{uc}$ and of mean $\overline{u}\,\overline{c}$ and turbulent $\overline{u'c'}$ counterpart. **b** Conservation of the total longitudinal mass flux Q^* per unit length (see Eq. 11)

turbulent terms exhibit a complex behaviour. Notably, the sign of the mean flux is intrinsically linked to the sign of the mean longitudinal velocity. Consequently, the mean flux is negative in the lower part of the recirculating region, where the mean flow is directed upwind relative to the source. The turbulent flux contributes negatively, a characteristic feature of turbulent dispersion in boundary flows (Marro et al. 2020; Lim and Vanderwel 2023; Vidali et al. 2025). As expected, the mean flux $\overline{u}\,\overline{c}$ dominates the total flux in terms of absolute value, with the turbulent contribution accounting for approximately 10% of the total flux. As a first step, these data are used to verify the downstream evolution of the normalised mass flux per unit length:

$$Q^* = \frac{1}{Q_{source}} \int_0^{+\infty} (\overline{u}\,\overline{c} + \overline{u'c'})\, dz, \tag{11}$$

where Q_{source} is the scalar emission per unit length of the source. The value of Q^*, expected to be equal to unity, serves as an indicator of the accuracy of the experimental setup, particularly regarding the transverse homogeneity of scalar emission at the source. A similar analysis, using the same source configuration but in a different flow typology (a turbulent boundary layer, without the presence of the square obstacle), was already carried out by Marro et al. (2020). The results presented in Fig. 7b show that in the near field, for $1.5H < x < 3.5H$, the value of Q^* remains approximately constant but exceeds unity by 28%. These deviations

near the source are likely due to insufficient spatial discretization of measurement points in this region, which is characterized by large concentration gradients and the presence of a recirculating flow. This leads to reduced precision in determining the various flux components. Conversely, further downstream, where the recirculating bubble progressively fades out, for $x > 4\,H$, the relative deviation from the expected value ($Q^* = 1$) is at most 10%. These findings highlight two key aspects: (i) the source setup provides a scalar flux that is homogeneously distributed along the transverse direction, and (ii) the statistical properties of the flow are independent of the transverse coordinate. In this sense, the flow and dispersion analyzed here can be considered statistically two-dimensional.

The simplest and most commonly used closure of the advection–diffusion equation in CFD codes directly relates the turbulent mass fluxes $\overline{u_j' c'}$ to the gradient of the mean concentration using a Standard Gradient-Diffusion Hypothesis (SGDH) relation of the type:

$$\overline{u_i' c'} = -D_{t,ij} \frac{\partial \overline{c}}{\partial x_{i,j}} \tag{12}$$

where $D_{t,ij}$ is the (diagonal) turbulent diffusion tensor. In its simplest formulation, the three-component tensor can be expressed as $D_{t,ij} = D_t \delta_{ij}$, therefore assuming isotropy of the coefficient of turbulent diffusion, usually estimated as the ratio between the turbulent viscosity ν_t and the turbulent Schmidt number Sc_t. The formulation of Eq. (12) relies in a well-established analogy with the molecular diffusion, and implies that there is a systematic opposition between the sign of the turbulent mass flux and the sign of the mean concentration gradient. It is however well known that, for what concerns the dispersion along the streamwise direction, this hypothesis does not hold (Fackrell and Robins 1982a; Marro et al. 2020). Figure 8a reports the vertical evolution of the quantities $\partial \overline{c}/\partial x$ and $\overline{u'c'}$. It can be observed that the sign opposition between the two terms is only satisfied in the recirculation zone and not in the rest of the domain. Since the turbulent diffusivity D_t is strictly positive, as it is defined as the ratio of two positive variables (ν_t and Sc_t), these results show that it is impossible to effectively reproduce the turbulent flux in the longitudinal direction throughout the entire domain using the SGDH model. To address and circumvent these limitations, Daly and Harlow (1970) proposed the Generalized Gradient-Diffusion Hypothesis (GGDH) model, which expresses the longitudinal turbulent mass flux using the relation:

$$\overline{u_i' c'} = -\alpha_{c,x}^{GGDH} \tau_c \overline{u_i' u_j'} \frac{\partial \overline{c}}{\partial x_j}, \tag{13}$$

which, in the two-dimensional flow analysed here, becomes:

$$\overline{u'c'} = -\alpha_{c,x}^{GGDH} \tau_c \left(\overline{u'^2} \frac{\partial \overline{c}}{\partial x} + \overline{u'w'} \frac{\partial \overline{c}}{\partial z} \right), \tag{14}$$

where $\alpha_{c,x}^{GGDH}$ is a constant and τ_c is a characteristic mixing time that can be assumed, as a first approximation, equal to the turbulent time scale (Marro et al. 2018; Bertagni et al. 2019), i.e. $\tau_c = k/\varepsilon$. The scatter plot in Fig. 8d reports $\overline{u'c'}$ as a function of $-\frac{k}{\varepsilon_R}\left(\overline{u'^2}\,\frac{\partial \overline{c}}{\partial x} + \overline{u'w'}\,\frac{\partial \overline{c}}{\partial z}\right)$. Despite a significant dispersion of data points ($R^2 = 0.5$), by means of a linear regression, the constant $\alpha_{c,x}^{GGDH}$ can be estimated equal to 0.4. To evaluate the sensitivity of this coefficient in relation to the final estimation of $\overline{u'c'}$, Fig. 8b depicts $\overline{u'c'}$ using three distinct values of $\alpha_{c,x}^{GGDH}$ (0.1, 0.2, and 0.4). While the general profile shape is accurately replicated downstream of the obstacle, the magnitude of the $\overline{u'c'}$ flux is not well approximated by the closure model.

In order to further increase the accuracy of the model, Abe and Suga (2001) proposed a higher-order closure (HO-GGDH) by using a product of double correlations of velocities to

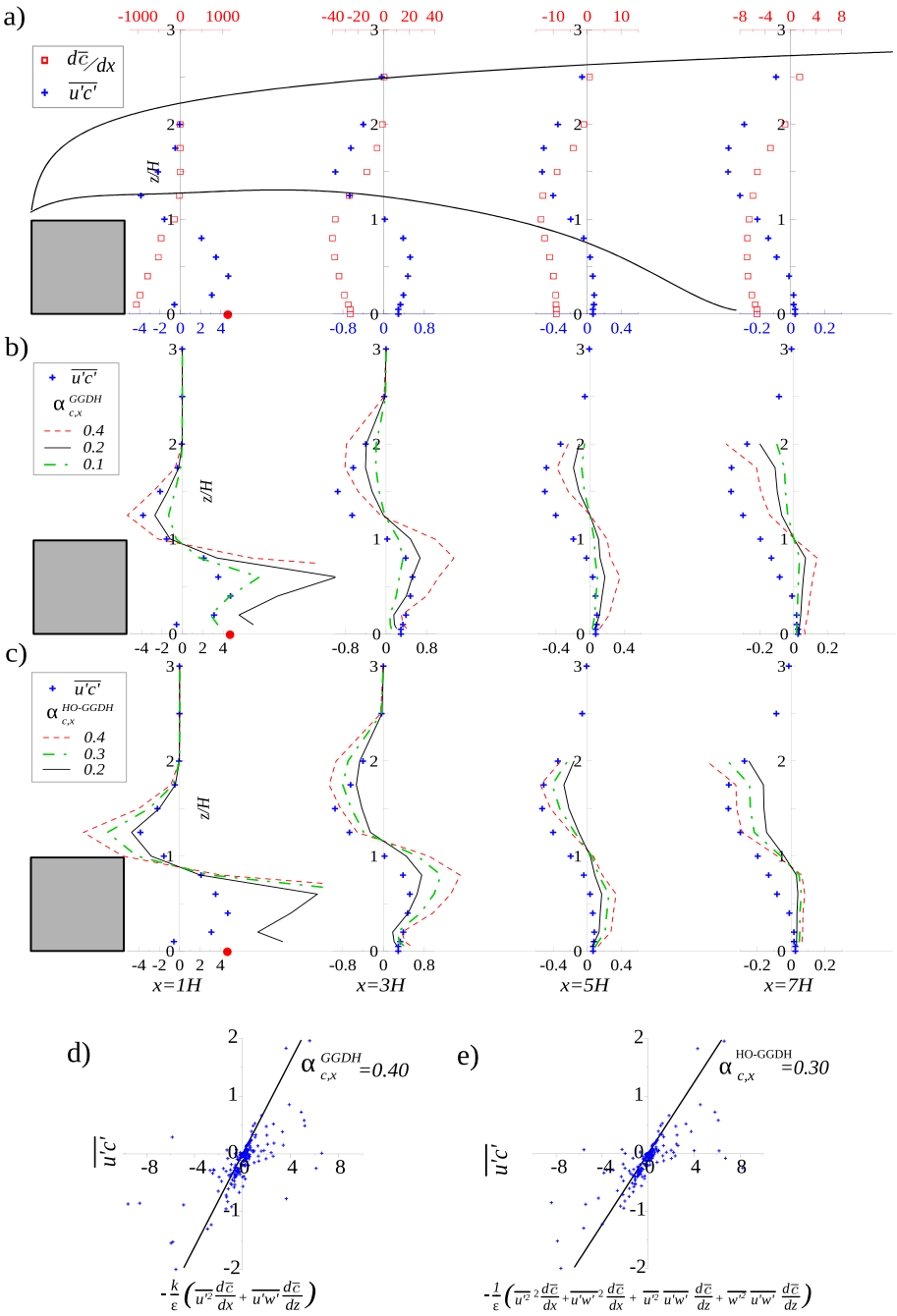

Fig. 8 **a** Spatial evolution of $\overline{u'c'}$ and $\partial\overline{c}/\partial x$. **b** Estimate of the turbulent horizontal mass flux with the GGDH closure model with different values of $\alpha_{c,x}^{\text{GGDH}}$. **c** Estimate of the turbulent horizontal mass flux with the HO-GGDH closure model with different values of $\alpha_{c,x}^{\text{HO-GGDH}}$. **d** Scatterplot for the determination of the coefficient $\alpha_{c,x}^{\text{GGDH}}$. **e** Scatterplot for the determination of the coefficient $\alpha_{c,x}^{\text{HO-GGDH}}$

express the diffusion coefficient $D_{t,ij}$. This closure is described by the following equation:

$$\overline{u_i' c'} = -\alpha_{c,x}^{HO-GGDH} \tau_c \frac{\overline{u_i' u_k'}\,\overline{u_k' u_j'}}{k} \frac{\partial \overline{c}}{\partial x_j}, \tag{15}$$

which, in the two-dimensional flow analysed here, writes:

$$\overline{u'c'} = -\alpha_{c,x}^{HO-GGDH} \frac{1}{\varepsilon} \left(\overline{u'^2}^2 \frac{\partial \overline{c}}{\partial x} + \overline{u'w'}^2 \frac{\partial \overline{c}}{\partial x} + \overline{u'^2}\,\overline{u'w'} \frac{\partial \overline{c}}{\partial z} + \overline{w'^2}\,\overline{u'w'} \frac{\partial \overline{c}}{\partial z} \right). \tag{16}$$

By conducting the same analysis as for the GGDH model, we observe (see Fig. 8e) a slight improvement in the results with a lower dispersion of data points ($R^2 = 0.63$). The determination of the coefficient $\alpha_{c,x}^{HO-GGDH}$, using linear regression, gives $\alpha_{c,x}^{HO-GGDH} = 0.3$. The sensitivity analysis (Fig. 8c) regarding this value on the final result highlights the same observations as for the GGDH model, namely a good representation of the profile shape together with difficulties in reproducing the intensity of the turbulent flux.

This analysis reveals that the SGDH model is internally inconsistent in the longitudinal direction because it fails to meet the condition of sign opposition between the turbulent mass flux and the longitudinal gradient of the mean concentration. The more complex closure models GGDH and HO-GGDH, which are not limited by this strict condition and benefiting from the inclusion of terms involving the vertical gradient of the concentration, provide estimates of $\overline{u'c'}$ that closely resemble the measured curves. It is worth noting, however, that the scatter plot in Fig. 8d for the GGDH model exhibits a moderate correlation coefficient ($R^2 = 0.5$), which reflects a significant dispersion in the data points. While the model offers a reasonable first-order approximation, these limitations highlight the challenges in accurately reproducing the turbulent flux. To quantify the impact of this dispersion on the coefficient estimation, sensitivity analyses (Fig. 8b and c) were conducted, demonstrating how variations in $\alpha_{c,x}^{GGDH}$ and $\alpha_{c,x}^{HO-GGDH}$ influence the model's predictions. Despite the slight improvement achieved with the HO-GGDH closure model ($R^2 = 0.63$, Fig. 8e), significant discrepancies remain between the predicted and measured turbulent fluxes. These discrepancies, with relative errors exceeding 100% in the estimation of maximum and minimum intensities of $\overline{u'c'}$, suggest that additional refinements to the closure models are necessary to better capture the underlying physics of turbulent diffusion processes.

3.5.2 Vertical Scalar Fluxes

Figure 9a simultaneously shows the spatial evolution of the vertical concentration gradient $\partial \overline{c}/\partial z$ and the turbulent vertical mass flux $\overline{w'c'}$. Unlike the longitudinal flux, the assumption of opposite signs between these two quantities is consistently upheld throughout the study domain. According to Eq. 12, we can therefore express the vertical turbulent mass fluxes as:

$$\overline{w'c'} = -D_{tz} \frac{\partial \overline{c}}{\partial z}, \tag{17}$$

where, to simplify notation, $D_{tz} = D_{t,zz}$. The simplest formulation of D_{tz} assumes a constant value throughout the domain. To verify the reliability of this assumption, we plot $\overline{w'c'}$ as a function of $\partial \overline{c}/\partial z$ in Fig. 9d. A best fit of the data provides a turbulent diffusivity equal to 0.006 m^2/s ($R^2 = 0.78$), a value (see Fig. 9b) that is likely to provide reliable estimates of the turbulent mass flux, except very close to the obstacle ($0.5H < x < 2H$ and $z < H$).

In order to take into account the spatial heterogeneity of the turbulent diffusion, it is customary to express it as the ratio of the turbulent viscosity ν_t, varying in space according to

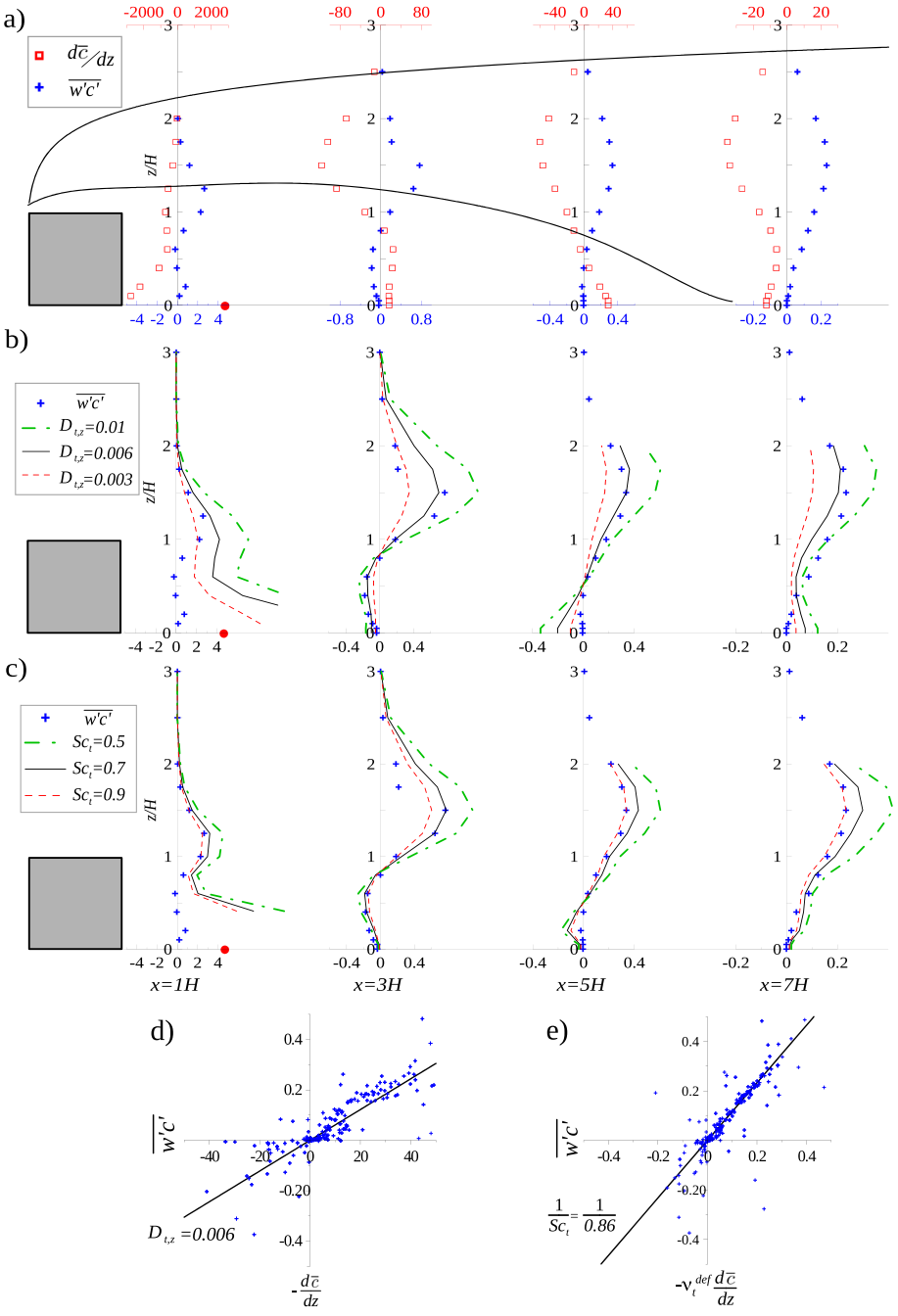

Fig. 9 **a** Spatial evolution of $\overline{w'c'}$ and $\partial\overline{c}/\partial z$. **b** Estimate of the turbulent vertical mass flux with the SGDH closure model with different values of the turbulent diffusivity D_t. **c** Estimate of the turbulent vertical mass flux with the SGDH closure model with different values of the turbulent Schmidt number (Sc_t). **d** Scatter plot for the determination of the turbulent diffusivity D_t. **e** Scatter plot for the determination of the turbulent Schmidt number (Sc_t)

its definition given by Eq. (1), and the turbulent Schmidt number Sc_t, assumed as a constant. As shown in Fig. 9e, where $\overline{w'c'}$ is plotted as a function of $\nu_t^{def} d\overline{c}/dz$, the dispersion of the experimental data points is significantly lower compared to panel d. Fitting the data with a linear regression provides $Sc_t \approx 0.86$, with a remarkably high correlation coefficient of $R^2 = 0.93$. In Fig. 9c, the sensitivity analysis performed to determine $\overline{w'c'}$ with different values of Sc_t (0.5, 0.7, and 0.9) illustrates that the value of $Sc_t = 0.9$ is suitable for the model, except in close proximity to the obstacle.

To complete our analysis, we evaluate the performances of more complex parametrisations already tested for $\overline{u'c'}$. The GGDH closure models express the vertical turbulent mass flux as:

$$\overline{w'c'} = -\alpha_{c,z}^{GGDH} \frac{k}{\varepsilon} \left(\overline{u'w'} \frac{\partial \overline{c}}{\partial x} + \overline{w'^2} \frac{\partial \overline{c}}{\partial z} \right). \tag{18}$$

Figure 10c shows $\overline{w'c'}$ as a function of $-\frac{k}{\varepsilon}\left(\overline{u'w'}\frac{\partial \overline{c}}{\partial x} + \overline{w'^2}\frac{\partial \overline{c}}{\partial z}\right)$. The linear regression provides a coefficient $\alpha_{c,z}^{GGDH} = 0.19$, with a correlation coefficient $R^2 = 0.4$. This relatively low value, much smaller than that obtained for the SGDH model, reflects significant data dispersion and underscores the uncertainty associated with the extracted coefficient $\alpha_{c,z}^{GGDH}$. This suggests that the GGDH model is less reliable for accurately capturing vertical turbulent fluxes compared to the SGDH model. Figure 10a, which shows the sensitivity analysis of the flux estimation for different values of the coefficient $\alpha_{c,z}^{GGDH}$, illustrates in a different form that, despite its increased complexity, the GGDH model does not provide a better estimation of $\overline{w'c'}$ compared to the SGDH model. On the contrary, it significantly worsens the results.

According to Eq. (15), assuming the High-Order GGDH (HO-GGDH) model, the vertical turbulent mass flux writes:

$$\overline{w'c'} = -\alpha_c^{HO-GGDH} \frac{1}{\varepsilon} \left(\overline{u'^2}\,\overline{u'w'} \frac{\partial \overline{c}}{\partial x} + \overline{w'^2}\,\overline{u'w'} \frac{\partial \overline{c}}{\partial x} + \overline{u'w'}^2 \frac{\partial \overline{c}}{\partial z} + \overline{u'^2} \frac{\partial \overline{c}}{\partial z} \right). \tag{19}$$

The estimate of the optimal value for the coefficient provides $\alpha_c^{HO-GGDH} \approx 0.08$ (see Fig. 10d), with a lower dispersion of the data points ($R^2 = 0.67$) compared to the GGDH model. Furthermore, the sensitivity analysis of the flux $\overline{w'c'}$ for different values of $\alpha_c^{HO-GGDH}$ demonstrates an improvement in the results compared to the GGDH model, although they are still not as accurate as those achieved with the SGDH model.

This analysis shows that all three models fail in estimating $\overline{w'c'}$ just downstream of the obstacle, $0.5H < x < 2H$ and $z < H$, a limitation, that may be partially due to the coarse spatial discretisation of the data in the very near field of the source, where concentration gradients are particularly steep. Moving away from the obstacle, there is a significant improvement in the results, even within the recirculating flow region. It is remarkable how, despite its simplicity, the SGDH model (with constant D_t) performs better than the GGDH and HO-GGDH models in most of the domain. However, the most robust model is undoubtedly the SGDH model $D_t = \nu_t / Sc_t$, with a turbulent Schmidt number close to unity, i.e. $Sc_t = 0.9$.

3.6 Concentration Variance Budget

As a final step, we focus on the budget of the concentration variance $\overline{c'^2}$, with focus on the spatial variability of its dissipation rate ε_c and its modelling as a function of local flow

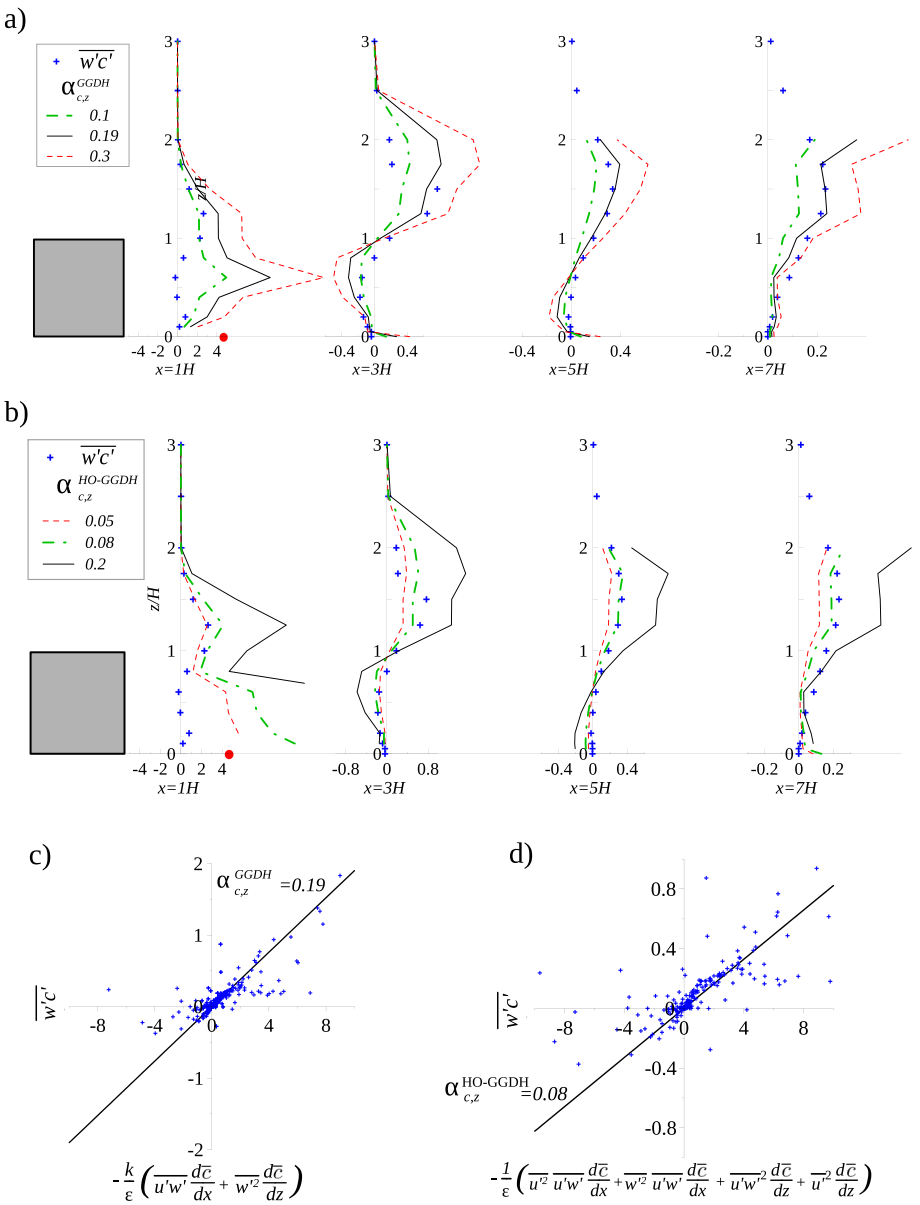

Fig. 10 **a** Estimate of the turbulent vertical mass flux with the GGDH closure model with different values of $\alpha_{c,z}^{\mathrm{GGDH}}$. **b** Estimate of the turbulent vertical mass flux with the HO-GGDH closure model with different values of $\alpha_{c,z}^{\mathrm{HO\text{-}GGDH}}$. **c** Scatterplot for the determination of the coefficient $\alpha_{c,z}^{\mathrm{GGDH}}$. **d** Scatterplot for the determination of the coefficient $\alpha_{c,z}^{\mathrm{HO\text{-}GGDH}}$

statistics. The balance equation of the concentration variance writes:

$$\underbrace{\frac{1}{2}\overline{u_j}\frac{\partial \overline{c'^2}}{\partial x_j}}_{Adv_{\overline{c'^2}}} = \underbrace{-\overline{u_j' c'}\frac{\partial \overline{c}}{\partial x_j}}_{P_{\overline{c'^2}}} \underbrace{-\frac{1}{2}\frac{\partial \overline{c'c'u_j'}}{\partial x_j}}_{-\frac{1}{2}\nabla\cdot T_{\overline{c'^2}}} - \underbrace{D_m \overline{\frac{\partial c'}{\partial x_j}\frac{\partial c'}{\partial x_j}}}_{\varepsilon_{\overline{c'^2}},} \tag{20}$$

where D_m is the molecular diffusion coefficient. The terms $Adv_{\overline{c'^2}}$, $P_{\overline{c'^2}}$, $T_{\overline{c'^2}}$, and $\varepsilon_{\overline{c'^2}}$ correspond to the advection by the mean velocity field, the production rate, the diffusion due to turbulent transport, and the dissipation rate of concentration variance, respectively. The first three terms of the balance can be directly estimated from the experimental data. To this aim, we first fitted the concentration measurements along z and x using a double Gaussian function for the vertical direction and a double exponential function for the longitudinal direction. In this way, we reduced the errors from the spatial discretization of the gradients. As for the dissipation rate of t.k.e., the direct estimate of the scalar variance dissipation rate ($\varepsilon_{\overline{c'^2}}$) is challenging, since it requires measuring instantaneous concentration gradients at the Corrsin scale (Corrsin 1958). Differently from ε, we can obtain an exact estimate as a residual of the budget (20). Here, the term 'exact estimate' refers to an estimate that may be subject to numerical errors when evaluating the terms that make up the budget, but it is not influenced by assumptions about the contribution of different terms (as was the case for ε_R, obtained assuming as negligible the pressure term in Eq. 2).

Figure 11a presents the spatial evolution of the different terms of the budget (Eq. 20). Between the obstacle and the source ($0.5H < x < 1.5H$), the maxima of the quantities are located close to the ground, while for more distant profiles, the maxima are located in the high-shear zone ($H < z < 2H$). For $x > 1.5H$ and outside Zone I, there is an equilibrium between $\varepsilon_{\overline{c'^2}}$ and $Adv_{\overline{c'^2}}$, which have a larger amplitude than the terms of production ($P_{\overline{c'^2}}$) and transport ($T_{\overline{c'^2}}$). In the recirculation zone and for $x > 1.5H$, differently from Zone II, the transport term is positive.

Disposing of a reference estimate of $\varepsilon_{\overline{c'^2}}$, we can use it as a benchmark to test the reliability of its most common closure models adopted in the literature. According to Csanady (1967) $\varepsilon_{\overline{c'^2}}$ can be linked to the concentration variance $\overline{c'^2}$ as:

$$\varepsilon_{\overline{c'^2}} = \frac{\overline{c'^2}}{T_c}, \tag{21}$$

through a typical mixing time scale T_c (Sykes et al. 1984; Hsieh et al. 2007; Ferrero et al. 2017) which Andronopoulos et al. (2001) have expressed as:

$$T_c = \frac{L_c}{k^{1/2}}, \tag{22}$$

where L_c is a length scale of the concentration fluctuations. Alternatively, T_c can be expressed as proportional to the characteristic turbulent time k/ε, which leads to (CEREA 2011; Milliez and Carissimo 2008b):

$$\varepsilon_{\overline{c'^2}} = \frac{1}{R_f}\frac{\varepsilon}{k}\overline{c'^2}, \tag{23}$$

where R_f is a constant, whose value, to be determined experimentally, is assumed to be included between a lower $R_f = 0.5$ (Hsieh et al. 2007) and an upper bound $R_f = 0.8$ (Sato and Sada 2002).

To investigate this feature, we plot in Fig. 11c the term $\frac{\varepsilon}{k}\overline{c'^2}$ as a function of the scalar variance dissipation rate $\varepsilon_{\overline{c'^2}}$. By performing a linear regression, we obtain $R_f = 0.66$, which

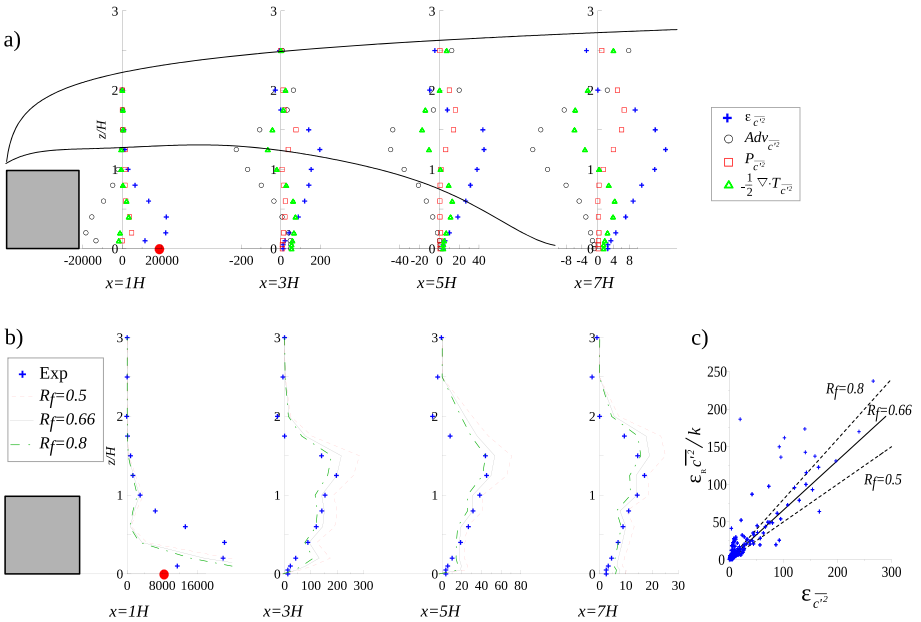

Fig. 11 **a** Terms of the balance for the concentration variance. **b** Estimate of the dissipation of concentration variance as a function of the coefficient R_f. c) Scatterplot for the determination of the coefficient R_f

falls between the values 0.8 and 0.5 used by Sato and Sada (2002) and Hsieh et al. (2007), respectively. The correlation coefficient of the linear regression is $R^2 = 0.84$, indicating a strong linear relationship between the estimated and experimentally determined values of the dissipation rate of concentration variance. This relatively high R^2 value demonstrates that the closure model for $\varepsilon_{\overline{c'^2}}$ effectively captures the dissipation dynamics in the majority of the domain. However, the model does not completely eliminate the variability observed in the data, as reflected in the dispersion of the data points in the scatter plot. Figure 11b reports a sensitivity analysis of the model results with respect to a variation in the coefficient R_f, ranging from 0.5 to 0.8. The dissipation of concentration variance ($\varepsilon_{\overline{c'^2}}$) can be reliably estimated in the whole domain except near the obstacle at $x = H$, where such analysis would require a higher spatial density of measurement points, to reliably characterise concentration gradients close to the source.

4 Conclusions

We conducted a detailed experimental characterization of turbulent flow and pollutant dispersion around a two-dimensional square obstacle in a turbulent boundary layer. The flow dynamics revealed a recirculation zone downstream of the obstacle, with an average length of $6H$, where high shear leads to increased turbulent viscosity and momentum fluxes compared to the incident boundary layer. We assessed the turbulence kinetic energy budget, estimating the dissipation rate, and compared this with traditional methods based on turbulence isotropy and the Taylor hypothesis, revealing their limitations within the wake region.

Estimates of the Eulerian length scale L, obtained through two-point correlation PIV measurements, provided insights into the spatial structure of the flow. These estimates, together with those of t.k.e. intensity and dissipation rate, were used to test parametrizations for L based on the assumption of local dynamical equilibrium, commonly employed in RANS and pollutant dispersion models.

The dispersion of pollutants was studied downstream of the obstacle, with our results indicating that the Lognormal distribution best models concentrations within the recirculating zone, while the Gamma distribution is more accurate outside it.

Experimental estimates of turbulent mass fluxes were used to test the internal consistency of various closure models (SGDH, GGDH, and HO-GGDH) for the advection–diffusion equation. We demonstrated that the SGDH model fails to accurately estimate horizontal mass fluxes due to the inconsistent sign relationship between $\overline{u'c'}$ and the longitudinal gradient of mean concentration. The adoption of more advanced and comprehensive models, such as GGDH and HO-GGDH, yields a close approximation of the spatial trend of $\overline{u'c'}$, although it falls short in accurately estimating the intensity values. In the context of turbulent vertical mass fluxes, the SGDH model demonstrated itself to be the most robust approach.

Our analysis also led to the determination of the turbulent diffusivity coefficient D_t and turbulent Schmidt number Sc_t, confirming that RANS models using constant Sc_t values satisfactorily reproduce mass fluxes. Additionally, we evaluated the concentration variance equation and the validity of closure models for its dissipation rate.

We identified a gap in the spatial resolution of measurements near the pollutant source, particularly at positions $0.5H < x < 2H$ and $z < H$, suggesting that additional measurements in this region could enhance understanding of physical processes and improve model validation. This experimental work could also be extended to more complex geometries, such as 3D flows around a single obstacle or within an obstacle network.

On the numerical side, our database provides a benchmark for evaluating more sophisticated turbulence and dispersion models, including LES, DNS, Lattice Boltzmann, and Lagrangian approaches, offering valuable insights for future modeling improvements in atmospheric dispersion studies.

Funding Open access funding provided by Politecnico di Torino within the CRUI-CARE Agreement.

References

Abe K, Suga K (2001) Towards the development of a reynolds-averaged algebraic turbulent scalar-flux model. Int J Heat Fluid Flow 22(1):19–29

Andronopoulos S, Grigoriadis D, Robins A, Venetsanos A, Rafailidis S, Bartzis J (2001) Three-dimensional modelling of concentration fluctuations in complicated geometry. Environ Fluid Mech 1:415–440

Baldi S, Yianneski M (2004) On the quantification of energy dissipation in the impeller stream of a stirred vessel from fluctuating velocity gradient measurements. Chem Eng Technol 59(13):2659–2671

Baldi S, Ducci A, Yianneski M (2004) Determination of dissipation rate in stirred vessels through direct measurement of fluctuating velocity gradients. Chem Eng Technol 27–3:275–281

Benedict LH, Gould RD (1996) Towards better uncertainty estimates for turbulence statistics. Exp Fluids 22:129. https://doi.org/10.1007/s003480050030
Bertagni MB, Marro M, Salizzoni P, Camporeale C (2019) Solution for the statistical moments of scalar turbulence. Phys Rev Fluids 4(124):701. https://doi.org/10.1103/PhysRevFluids.4.124701
Bewley GP, Chang K, Bodenschatz E, et al. (2012) On integral length scales in anisotropic turbulence. Phys Fluids 24(6)
Boussinesq J (1877) Essai sur la théorie des eaux courantes. Impr. nationale
Carpentieri M, Hayden P, Robins AG (2012) Wind tunnel measurements of pollutant turbulent fluxes in urban intersections. Atmos Environ 46:669–674
Carpentieri M, Hayden P, Robins AG (2012) Wind tunnel measurements of pollutant turbulent fluxes in urban intersections. Atmos Environ 46:669–674
Carpentieri M, Robins AG, Hayden P, Santi E (2018) Mean and turbulent mass flux measurements in an idealised street network. Environ Pollut 234:356–367
Cassiani M (2013) The volumetric particle approach for concentration fluctuations and chemical reactions in lagrangian particle and particle-grid models. Bound-Layer Meteorol 146(2):207–233. https://doi.org/10.1007/s10546-012-9752-3
Cassiani M, Franzese P, Giostra U (2005) A pdf micromixing model of dispersion for atmospheric flow. part i development of the model, application to homogeneous turbulence and to neutral boundary layer. Atmos Environ 39(8):1457–1469
Cassiani M, Bertagni MB, Marro M, Salizzoni P (2020) Concentration fluctuations from localized atmospheric releases. Bound-Layer Meteorol 177(2):461–510
CEREA (2011) Code Saturne 2.0.4 Theory and Programmers Guide
Charlwood S, Frank D, Wykes MD (2023) The influence of buoyancy upon pollution trapping and dispersal in the wake of a backward-facing step. Flow 3:E21
Comte-Bellot G, Bailly C (2003) Turbulence
Corrsin S (1958) Local isotropy in turbulent shear flow. Tech rep
Counihan J, Hunt J, Jackson P (1974) Wakes behind two-dimensional surface obstacles in turbulent boundary layers. J Fluid Mech 64(3):529–564
Csanady G (1967) Concentration fluctuations in turbulent diffusion. J Atmos Sci 24(1):21–28
Daly BJ, Harlow FH (1970) Transport equations in turbulence. Phys Fluids 13(11):2634–2649
Del Ponte AV, Fellini S, Marro M, van Reeuwijk M, Ridolfi L, Salizzoni P (2024) Influence of street trees on turbulent fluctuations and transport processes in an urban canyon: a wind tunnel study. Bound-Layer Meteorol 190(2):6
Di Bernardino A, Monti P, Leuzzi G, Querzoli G (2020) Turbulent schmidt number measurements over three-dimensional cubic arrays. Bound-Layer Meteorol 174(2):231–250
Fackrell J (1980) A flame ionisation detector for measuring fluctuating concentration. J Phys E: Sci Instrum 13(8):888
Fackrell J, Robins A (1982) Three-dimensional modeling of concentration fluctuations in complicated geometry. J Fluid Mech 117:1–26
Fackrell JE, Robins A (1982) Concentration fluctuations and fluxes in plumes from point sources in a turbulent boundary layer. J Fluid Mech 117:1–26
Fellini S, Ridolfi L, Salizzoni P (2020a) Street canyon ventilation: combined effect of cross-section geometry and wall heating. Q J R Meteorol Soc
Fellini S, Salizzoni P, Ridolfi L (2020) Centrality metric for the vulnerability of urban networks to toxic releases. Phys Rev E 101(3):032
Fellini S, Salizzoni P, Ridolfi L (2021) Vulnerability of cities to toxic airborne releases is written in their topology. Sci Rep 11(1):23
Fellini S, Marro M, Del Ponte AV, Barulli M, Soulhac L, Ridolfi L, Salizzoni P (2022) High resolution wind-tunnel investigation about the effect of street trees on pollutant concentration and street canyon ventilation. Build Environ 226(109):763
Ferrero E, Mortarini L, Purghè F (2017) A simple parametrization for the concentration variance dissipation in a lagrangian single-particle model. Bound-Layer Meteorol 163:91–101
Finardi S, Tinarelli G, Faggian P, Brusasca G (1998) Evaluation of different wind field modeling techniques for wind energy applications over complex topography. J Wind Eng Ind Aerodyn 74–76:283–294. https://doi.org/10.1016/S0167-6105(98)00025-7
Finn D, Clawson KL, Carter RG, Rich JD, Biltoft C, Leach M (2010) Analysis of urban atmosphere plume concentration fluctuations. Bound-Layer Meteorol 136:431–456
Gorlé C, van Beeck J, Rambaud P (2010) Dispersion in the wake of a rectangular building: validation of two Reynolds-averaged Navier-Stokes modelling approaches. Bound-Layer Meteorol 137:115–133
Hinze J (1975) Turbulence, 2nd edn. McGraw-Hill, New York

Hsieh KJ, Lien FS, Yee E (2007) Numerical modeling of passive scalar dispersion in an urban canopy layer. J Wind Eng Ind Aerodyn 95(12):1611–1636
Hunt J (1971) A theory for the laminar wake of a two-dimensional body in a boundary layer. J Fluid Mech 49(1):159–178
Irwin H (1981) The design of spires for wind simulation. J Wind Eng Ind Aerodyn 7(3):361–366. https://doi.org/10.1016/0167-6105(81)90058-1
Kakosimos KE, Hertel O, Ketzel M, Berkowicz R (2010) Operational street pollution model (ospm)-a review of performed application and validation studies, and future prospects. Environ Chem 7(6):485–503
Koeltzsch K (2000) The height dependence of the turbulent schmidt number within the boundary layer. Atmos Environ 34(7):1147–1151
Kukačka L, Nosek Š, Kellnerová R, Jurčáková K, Jaňour Z, et al. (2012) Wind tunnel measurement of turbulent and advective scalar fluxes: a case study on intersection ventilation. The Scientific World Journal 2012
Launder B, Spalding D (1974) The numerical computation of turbulent flows. Comput Methods Appl Mech Eng 3(2):269–289
Li J, Bilger R (1996) The diffusion of conserved and reactive scalars behind line sources in homogeneous turbulence. J Fluid Mech 318:339–372
Li T, Fellini S, van Reeuwijk M (2023) Urban air quality: what is the optimal place to reduce transport emissions? Atmos Environ 292(119):432
Lim H, Vanderwel C (2023) Turbulent dispersion of a passive scalar in a smooth-wall turbulent boundary layer. J Fluid Mech 969:A26. https://doi.org/10.1017/jfm.2023.562
Liu X, Thomas F (2004) Measurement of the turbulent kinetic energy budget of a planar wake flow in pressure gradients. Exp Fluids 37:469–482
Longo R, Fürst M, Bellemans A, Ferrarotti M, Derudi M, Parente A (2019) Cfd dispersion study based on a variable schmidt formulation for flows around different configurations of ground-mounted buildings. Build Environ 154:336–347
Longo R, Bellemans A, Derudi M, Parente A (2020) A multi-fidelity framework for the estimation of the turbulent schmidt number in the simulation of atmospheric dispersion. Build Environ 185(107):066
Marro M, Salizzoni P, Cierco FX, Korsakissok I, Danzi E, Soulhac L (2014) Plume rise and spread in buoyant releases from elevated sources in the lower atmosphere. Environ Fluid Mech 14:201–219
Marro M, Nironi C, Salizzoni P, Soulhac L (2015) Dispersion of a passive scalar fluctuating plume in a turbulent boundary layer. part ii: Analytical modelling. Bound -Layer Meteorol 156(3):447–469. https://doi.org/10.1007/s10546-015-0041-9
Marro M, Salizzoni P, Soulhac L, Cassiani M (2018) Dispersion of a passive scalar fluctuating plume in a turbulent boundary layer. part iii: Stochastic modelling. Bound -Layer Meteorol 167(3):349–369. https://doi.org/10.1007/s10546-017-0330-6
Marro M, Gamel H, Méjean P, Correia H, Soulhac L, Salizzoni P (2020) High-frequency simultaneous measurements of velocity and concentration within turbulent flows in wind-tunnel experiments. Exp Fluids 61(12):1–13
Michelet S, Antoine Y, Lemoine F, Mahouast M (1998) Mesure directe du taux de dissipation de l'énergie cinétique de turbulence par vélocimétrie laser bi-composante : validation dans une turbulence de grille. Comptes rendus de l'Académie des sciences Série IIb, mécanique, physique, astronomie 326:621–626
Milliez M, Carissimo B (2008) Computational fluid dynamical modelling of concentration fluctuations in an idealized urban area. Bound -Layer Meteorol 127:241–259
Milliez M, Carissimo B (2008) Computational fluid dynamical modelling of concentration fluctuations in an idealized urban area. Bound-Layer Meteorol 127:241–259
Mochida A, Tominaga Y, Murakami S, Yoshie R (2002) Comparison of various k-eps model and dsm applied to flow around a high-rise building, report on aij cooperative project for cfd prediction of wind environment. Wind Struct 2–4:227–244
Moonen P, Dorer V, Carmeliet J (2011) Evaluation of the ventilation potential of court yards and urban street canyons using rans and les. J Wind Eng Ind Aerodyn 99:414–423
Nironi C (2013) Concentration fluctuations of a passive scalar in a turbulent boundary layer. Theses, Ecole Centrale de Lyon
Nironi C, Salizzoni P, Marro M, Mejean P, Grosjean N, Soulhac L (2015) Dispersion of a passive scalar fluctuating plume in a turbulent boundary layer. part i: Velocity and concentration measurements. Bound-Layer Meteorol 156(3):415–446
Nosek Š, Kukačka L, Jurčáková K, Kellnerová R, Jaňour Z (2017) Impact of roof height non-uniformity on pollutant transport between a street canyon and intersections. Environ Pollut 227:125–138
Oettl D, Ferrero E (2017) A simple model to assess odour hours for regulatory purposes. Atmos Environ 155:162–173

Pavageau M, Schatzmann M (1999) Wind tunnel measurements of concentration fluctuations in an urban street canyon. Atmos Environ 33(24–25):3961–3971
Poggi D, Katul G, Albertson J (2006) Scalar dispersion within a model canopy: measurements and three-dimensional lagrangian models. Adv Water Resour 29(2):326–335
Pope SB (2000) Turbulent flows. Cambridge University Press
Raffel M, Willert CE, Kompenhans J et al (1998) Particle image velocimetry: a practical guide, vol 2. Springer, Berlin
Raupach MR, Legg BJ (1983) Turbulent dispersion from an elevated line source: measurements of wind-concentration moments and budgets. J Fluid Mech 136:111–137
Ravina M, Panepinto D, Mejia Estrada J, De Giorgio L, Salizzoni P, Zanetti M, Meucci L (2020) Integrated model for estimating odor emissions from civil wastewater treatment plants. Environ Sci Pollut Res 27:3992–4007
Rodi W (1997) Comparison of les and rans calculations of the flow around bluff bodies. J Wind Eng Ind Aerodyn 69–71:55–75
Rossi R (2010) A numerical study of algebraic flux models for heat and mass transport simulation in complex flows. Int J Heat Mass Transf 53(21–22):4511–4524
Rossi R, Iaccarino G (2009a) Numerical simulation of scalar dispersion downstream of a square obstacle using gradient transport type models. Atmospheric Environment pp 1–14
Rossi R, Iaccarino G (2009) Numerical simulation of scalar dispersion downstream of a square obstacle using gradient-transport type models. Atmos Environ 43(16):2518–2531
Rossi R, Philips D, Iaccarino G (2010) A numerical study of scalar dispersion downstream of a wall-mounted cube using direct simulations and algebraic flux models. Int J Heat Fluid Flow 31(5):805–819
Sabatino SD, Buccolieri R, Pulvirenti B, Britter R (2007) Simulation of pollutant dispersion within idealised urban-type geometries with cfd and integral models. Atmos Environ 41:8316–8329
Sabatino SD, Buccolieri R, Pulvirenti B, Britter R (2008) Flow and pollutant dispersion in street canyons using fluent and adms-urban. Environ Model Assess 13:369–381
Salizzoni P, Soulhac L, Mejean P (2009) Street canyon ventilation and atmospheric turbulence. Atmos Environ 43(32):5056–5067
Salizzoni P, Marro M, Soulhac L, Grosjean N, Perkins RJ (2011) Turbulent transfer between street canyons and the overlying atmospheric boundary layer. Bound-Layer Meteorol 141(3):393–414
Salizzoni P, Vaux S, Creyssels M, Amielh M, Pietri L, Anselmet F (2023) Turbulent transfer and entrainment in a low-density jet. J Fluid Mech 968:A27. https://doi.org/10.1017/jfm.2023.464
Sato A, Sada K (2002) Estimation of gas concentration fluctuations using a numerical model and comparison with those of wind tunnel experiments. In: Proceedings, 8th Int. Conf. on Harmonisation within atmospheric dispersion modelling for regulatory purposes, pp 215–219
Schanderl W, Jenssen U, Strobl C, Manhart M (2017) The structure and budget of turbulent kinetic energy in front of a wall-mounted cylinder. J Fluid Mech 827:285–321. https://doi.org/10.1017/jfm.2017.486
Schmitt FG (2007) About boussinesq's turbulent viscosity hypothesis: historical remarks and a direct evaluation of its validity. Comptes Rendus Mécanique 335(9–10):617–627
Schofield WH, Logan E (1990) Turbulent shear flow over surface mounted obstacles. J Fluids Eng 112(4):376–385
Sciacchitano A, Wieneke B (2016) Piv uncertainty propagation. Meas Sci Technol 27(8):084
Snijders A, Koppius A, Nieuwvelt C (1983) An experimental determination of the turbulent prandtl number in the inner boundary layer for air flow over a flat plate. Int J Heat Mass Transf 26:425–431
Soulhac L, Salizzoni P, Cierco FX, Perkins R (2011) The model SIRANE for atmospheric urban pollutant dispersion; part I, presentation of the model. Atmos Environ 45(39):7379–7395
Soulhac L, Salizzoni P, Mejean P, Didier D, Rios I (2012) The model sirane for atmospheric urban pollutant dispersion; part ii, validation of the model on a real case study. Atmos Environ 49:320–337
Soulhac L, Nguyen CV, Volta P, Salizzoni P (2017) The model sirane for atmospheric urban pollutant dispersion. part iii: Validation against no2 yearly concentration measurements in a large urban agglomeration. Atmos Environ 167:377–388
Stapountzis H, Sawford BL, Hunt J, Britter RE (1986) Structure of the temperature field downwind of a line source in grid turbulence. J Fluid Mech 165:401–424
Sykes R, Lewellen W, Parker S (1984) A turbulent-transport model for concentration fluctuations and fluxes. J Fluid Mech 139:193–218
Takimoto H, Inagaki A, Kanda M, Sato A, Michioka T (2013) Length-scale similarity of turbulent organized structures over surfaces with different roughness types. Boundary-Layer Meteorol 147:217–236
Tominaga Y, Stathopoulos T (2013) Cfd simulation of near-field pollutant dispersion in the urban environment: review of current modeling techniques. Atmos Environ 79:716–730
Townsend A (1976) The structure of turbulent shear flow. Cambridge University Press, Cambridge

Tritton D (1974) Physical Fluid Dynamics
Vidali C, Marro L, Gostiaux L, Houssin D, Vyazmina E, Salizzoni P (2025) Wind-tunnel experiment of heavy gas and passive scalar emission in a turbulent boundary layer. submitted to Boundary-Layer Meterology
Vinçont JY, Simoëns S, Ayrault M, Wallace J (2000) Passive scalar dispersion in a turbulent boundary layer from a line source at the wall and downstream of an obstacle. J Fluid Mech 424:127–167
Weil J, Sykes R, Venkatram A (1992) Evaluating air-quality models: review and outlook. J Appl Meteorol 31:1121–1145
Westerweel J (1997) Fundamentals of digital particle image velocimetry. Meas Sci Technol 8(12):1379
Xie Z, Castro I (2006) Les and rans for turbulent flow over arrays of wall mounted obstacles. Flow Turbulence Combust 76:21–312
Yaghoubi M, Zamankhan P, Sabzevari A (1998) Numerical analysis of two-dimensional wind flow in and around rectangular buildings part i: Modelling and simulation. Wind Engineering pp 81–97
Yassin MF (2008) Probability characteristics of concentration fluctuations in plume dispersal. JES J Eng Sci 36(1):115–130
Yin G, Andersen M, Ong MC (2020) Numerical simulations of flow around two tandem wall-mounted structures at high reynolds numbers. Appl Ocean Res 99(102):124
Zhao Y, Chew LW, Fan Y, Gromke C, Hang J, Yu Y, Ricci A, Zhang Y, Xue Y, Fellini S et al (2023) Fluid tunnel research for challenges of urban climate. Urban Clim 51(101):659